

Journal of Geophysical Research: Oceans

RESEARCH ARTICLE

10.1002/2017JC013409

Special Section:

The Southern Ocean Carbon and Climate Observations and Modeling (SOCCOM) Project: Technologies, Methods, and Early Results

Key Points:

- Upwelling of deep water is largely isopycnal in the Southern Ocean interior even at topographic upwelling hot spots
- Atlantic and Indian Deep Waters cool and freshen significantly along interior isopycnals, homogenizing deep water
- Significant transformation to lighter densities occurs below the mixed layer due to mixing with fresher surface waters

Correspondence to:

V. Tamsitt,
vtamsitt@ucsd.edu

Citation:

Tamsitt, V., Abernathay, R. P., Mazloff, M. R., Wang, J., & Talley, L. D. (2018). Transformation of deep water masses along Lagrangian upwelling pathways in the Southern Ocean. *Journal of Geophysical Research: Oceans*, 123, 1994–2017. <https://doi.org/10.1002/2017JC013409>

Received 5 SEP 2017

Accepted 7 DEC 2017

Published online 14 MAR 2018

Transformation of Deep Water Masses Along Lagrangian Upwelling Pathways in the Southern Ocean

V. Tamsitt¹ , R. P. Abernathay² , M. R. Mazloff¹ , J. Wang³, and L. D. Talley¹ 

¹Scripps Institution of Oceanography, University of California San Diego, La Jolla, CA, USA, ²Lamont Doherty Earth Observatory, Columbia University, Palisades, NY, USA, ³Jet Propulsion Laboratory, California Institute of Technology, Pasadena, CA, USA

Abstract Upwelling of northern deep waters in the Southern Ocean is fundamentally important for the closure of the global meridional overturning circulation and delivers carbon and nutrient-rich deep waters to the sea surface. We quantify water mass transformation along upwelling pathways originating in the Atlantic, Indian, and Pacific and ending at the surface of the Southern Ocean using Lagrangian trajectories in an eddy-permitting ocean state estimate. Recent related work shows that upwelling in the interior below about 400 m depth is localized at hot spots associated with major topographic features in the path of the Antarctic Circumpolar Current, while upwelling through the surface layer is more broadly distributed. In the ocean interior upwelling is largely isopycnal; Atlantic and to a lesser extent Indian Deep Waters cool and freshen while Pacific deep waters are more stable, leading to a homogenization of water mass properties. As upwelling water approaches the mixed layer, there is net strong transformation toward lighter densities due to mixing of freshwater, but there is a divergence in the density distribution as Upper Circumpolar Deep Water tends become lighter and dense Lower Circumpolar Deep Water tends to become denser. The spatial distribution of transformation shows more rapid transformation at eddy hot spots associated with major topography where density gradients are enhanced; however, the majority of cumulative density change along trajectories is achieved by background mixing. We compare the Lagrangian analysis to diagnosed Eulerian water mass transformation to attribute the mechanisms leading to the observed transformation.

1. Introduction

Eighty percent of the World Ocean deep water is thought to return to the surface in the Southern Ocean (Lumpkin & Speer, 2007; Talley, 2013). This upwelling of deep water plays an integral role in the global ocean uptake and redistribution of heat, carbon, and nutrients (Frölicher et al., 2015; Sarmiento et al., 2004). Additionally, the upwelling of relatively warm deep water in the Southern Ocean has been driving the recent accelerated mass loss of Antarctic ice sheets (Cook et al., 2016). Early theories of the global ocean overturning proposed that diapycnal mixing in the ocean interior was necessary to convert dense water formed at high latitudes to lighter surface waters (Munk, 1966; Munk & Wunsch, 1998), but direct measurements of mixing suggest that ocean mixing in the open ocean interior is an order of magnitude too small (Waterhouse et al., 2014). An alternative mechanism for returning deep water to the ocean surface with minimal mixing has emerged, via wind-driven upwelling along steeply tilted isopycnals in the Southern Ocean in the upper 2,000 m (Sloyan & Rintoul, 2001; Toggweiler & Samuels, 1998), while below this diapycnal mixing is key for upwelling of abyssal waters. Recent observational studies indicate that the reality lies somewhere between the no-mixing limit and upwelling driven entirely by diapycnal mixing (Katsumata et al., 2013; Watson et al., 2013), but the role of mixing in the upwelling of deep water in the Southern Ocean remains poorly constrained.

Southern Ocean circulation is unique due to the lack of meridional boundaries at the latitudes of Drake Passage, enabling the circum polar flowing Antarctic Circumpolar Current (ACC), linking the major ocean basins and allowing interbasin exchange of properties. Steeply tilted isopycnals facilitate isopycnal upwelling of Circumpolar Deep Water (CDW) to the surface of the Southern Ocean, where it is directly modified by surface buoyancy fluxes. Theoretical modeling shows that a strong adiabatic overturning cell in the Southern Ocean is possible with isopycnals outcropping in both hemispheres and negligible interior diapycnal mixing; all diapycnal processes in this paradigm occur within the ocean's surface layer (Wolfe & Cessi, 2011).

However, observational studies suggest that the interior ocean mixing is an important component of the Southern Ocean meridional overturning circulation (Garabato et al., 2004; Katsumata et al., 2013; Naveira Garabato et al., 2016; Sloyan & Rintoul, 2001). Near-bottom mixing in hot spots over rough seafloor topography (Ledwell et al., 2000; Polzin, 1997) can accomplish upwelling of the denser Lower Circumpolar Deep Water (LCDW) to lighter Upper Circumpolar Deep Water (UCDW). Additionally, some LCDW density classes outcrop along the Antarctic continental slope rather than at the surface, and thus intense mixing in the bottom boundary layer facilitates transformation of these density classes to lighter water masses (Ruan et al., 2017). However, most of this bottom boundary layer mixing occurs within 1,000 m of the bottom (Garabato et al., 2004; St. Laurent et al., 2012; Waterhouse et al., 2014), so away from the continental slope and shallow topographic features, it is not clear how important mixing is in upwelling of deep water in the 1,000–2,000 m depth range (Toggweiler & Samuels, 1998). Recent analysis of repeat observations across Drake Passage indicates that diapycnal mixing sustains the overturning in the upper 1,000 m and in the 1,000–2,000 m above the seafloor, while in between, isopycnal stirring dominates in the Antarctic Intermediate Water and Upper Circumpolar Deep Water (UCDW) density classes (Mashayek et al., 2017; Naveira Garabato et al., 2016).

While there are many observations characterizing local episodes of intense turbulent mixing at rough topography, these measurements are sparse and infrequent in time, making it difficult to scale this to the integrated diapycnal mixing that affects the large-scale overturning. Tracer release experiments are suited for addressing this question, but to date these efforts have been confined to regional studies, which are then extrapolated to the circumpolar Southern Ocean (Mashayek et al., 2017; Watson et al., 2013). Additionally, while there is evidence that diapycnal mixing in the interior of the Southern Ocean is elevated in hot spots associated with topography (Naveira Garabato et al., 2016; Ruan et al., 2017; Watson et al., 2013), these hot spots make up a relatively small fraction of the total volume of the deep Southern Ocean. Therefore, for an upwelling deep water parcel, it is not well understood how mixing at these hot spots contributes to the integrated density change along the path from the deep ocean to the surface. There are several different approaches applied to estimating regional mixing using finescale parameterizations (Kunze et al., 2006) and inverse methods (Zika et al., 2010). To date there are multiple globally constrained estimates of the contribution of mixing to the overturning circulation, including inverse methods (Ganachaud & Wunsch, 2000; Groeskamp et al., 2017; Sloyan & Rintoul, 2001) and finescale parameterizations from float profiles (Whalen et al., 2012). In addition to these methods, Lagrangian experiments in ocean general circulation models and state estimates can provide a complimentary perspective to the role of mixing in upwelling because of the ability to isolate large-scale density modification along upwelling deep water pathways (Döös et al., 2008; Ludicone et al., 2008a).

Recent Lagrangian model analyses show that this upwelling is spatially nonhomogeneous and is enhanced at hot spots associated with major topographic features (Tamsitt et al., 2017). Using Lagrangian particle tracking in three eddying ocean models, Tamsitt et al. (2017) traced pathways of deep water from between 1,000 and 3,500 m depth at 30°S in the Atlantic, Indian, and Pacific to the surface of the Southern Ocean. Upwelling water followed narrow pathways along each ocean boundary to the ACC, before spiraling upward and southward in the ACC (Figures 1a–1c). Tamsitt et al. (2017) found that upwelling of deep waters in the interior (shown at 1,000 m depth, which is representative of the interior up to 500 m depth) is concentrated in high EKE regions at or downstream of topography (Figure 1) and hypothesize that this concentrated upwelling is due to vigorous eddy activity facilitating enhanced cross-frontal exchange, carrying water southward and upward along tilted isopycnals. However, the role of diapycnal mixing in these upwelling pathways, particularly at the topographic upwelling hot spots, was not investigated.

In this work, building on Tamsitt et al. (2017), we employ an eddy-permitting ocean state estimate to address how deep water transforms along Southern Ocean interior upwelling pathways, and where diapycnal mixing processes are important along these pathways. We use a Lagrangian particle tracking approach to quantify the density changes along these pathways and determine where significant water mass transformation occurs due to diapycnal mixing in the ocean interior, removed from the strong influence of surface buoyancy fluxes. This Lagrangian approach is powerful because it is possible to track the cumulative effect of interior mixing on the density of a water mass from its deep water source to the surface, along Lagrangian trajectories. Additionally, we quantify temperature and salinity modifications individually to differentiate between isopycnal water mass modification and diapycnal mixing processes. We quantify the contribution from diapycnal mixing in upwelling hot spots associated with topography to the total

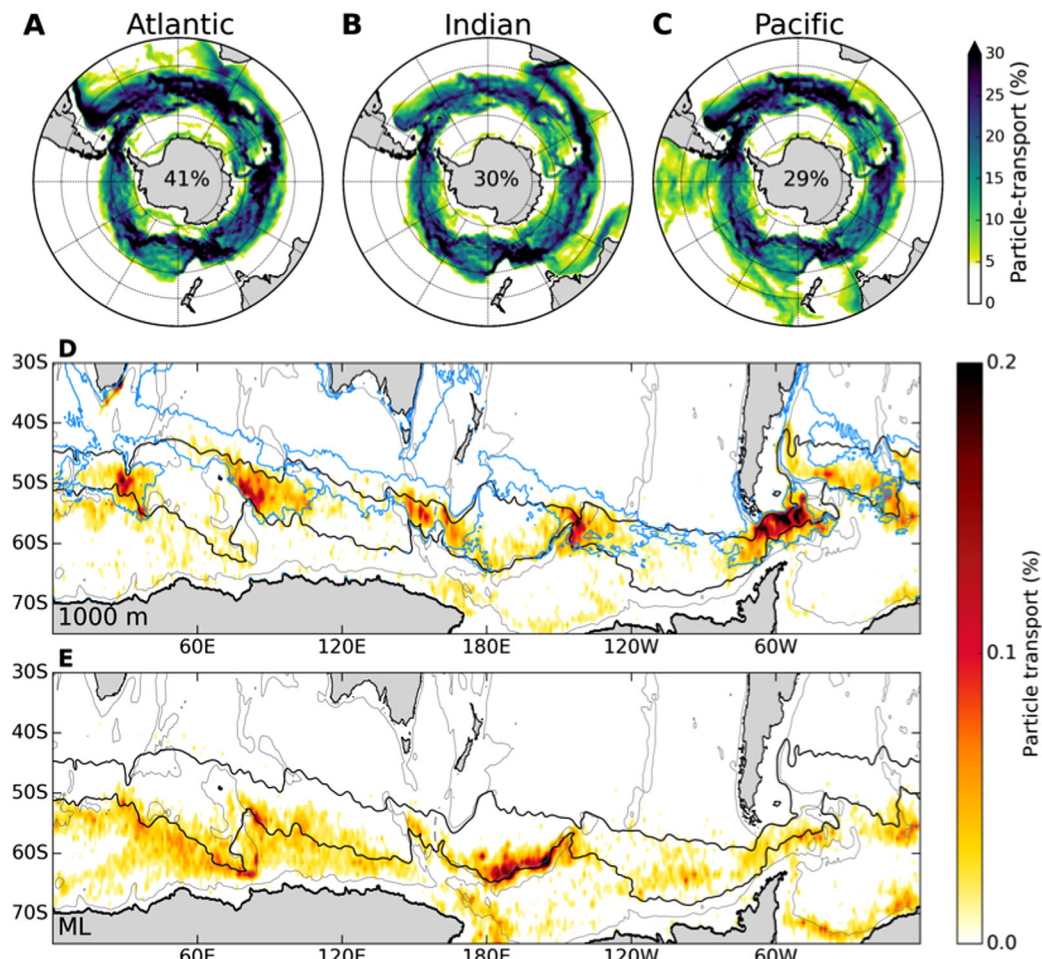


Figure 1. Maps of spatial patterns in Lagrangian upwelling in the Southern Ocean State Estimate, based on Tamsitt et al. (2017). Percent of particle-transport passing through each $1^\circ \text{ longitude} \times 1^\circ \text{ latitude}$ grid cell at any time between 30°S and the mixed layer for particles originating in the (a) Atlantic, (b) Indian, and (c) Pacific. (d) Percent of particle-transport crossing 1,000 m in each $1^\circ \text{ latitude} \times 1^\circ \text{ longitude}$ grid box between release at 30°S and the mixed layer in SOSE. Blue contours indicate regions where the mean surface EKE is greater than $100 \text{ cm}^2 \text{ s}^{-2}$. (e) Same as Figure 1d but for the ML crossing. Numbers on Antarctica in Figures 1a–1c show the percentage of the total upwelling particle-transport originating in the Atlantic, Indian or Pacific. Black lines in Figures 1d and 1e indicate the Northern and Southern boundaries of the ACC, from the outermost sea surface height contours closed through Drake Passage. Grey contours in Figures 1d and 1e show the 3,000 m bathymetry contour, highlighting major topographic features along the ACC.

diapycnal change. However, since some interior upwelling happens close to ridges and plateaus, elevated bottom mixing could be an important factor that is not included in the model analyzed here, and so we cannot evaluate its potential to increase diapycnal change in these locations. Finally, we relate Lagrangian density changes in the interior to diagnosed Eulerian diapycnal velocities in the interior to gain insight into the processes driving water mass transformation.

In section 2, we describe the model and Lagrangian and Eulerian methods of quantifying water mass transformation. The total transformation along Lagrangian trajectories are discussed in section 3.1, the contributions from temperature and salinity in section 3.2, and the spatial distribution of transformation in section 3.3. The results and conclusions are presented in section 4.

2. Model and Methods

2.1. The Southern Ocean State Estimate

The Southern Ocean State Estimate (SOSE) is an eddy-permitting, data-assimilating, ocean general circulation model based on the MITgcm (Mazloff et al., 2010). The model is configured in a domain from 24.7°S to

78°S with an open northern boundary, with 1/6° horizontal resolution and 42 uneven vertical levels, ranging from 10 m thickness at the sea surface to 250 m in the abyssal ocean. SOSE employs software developed by the consortium for Estimating the Climate and Circulation of the Ocean (ECCO; <http://www.ecco-group.org>) to assimilate the majority of available in situ observations using an adjoint method. Assimilated observations include, but are not limited to, Argo profiling float data, Global Ocean Ship-based Hydrographic Investigations Program (GO-SHIP) hydrographic data, Marine Mammals Observing the Ocean Pole to Pole (MEOP) CTD data, satellite-based sea surface height and sea surface temperature. The solution is optimized by minimizing a cost function, which is the uncertainty-weighted misfit of the model state and the observations. A 1° global state estimate (Forget, 2010) is used for the initial and northern open boundary conditions. The atmospheric state is initialized using the ECMWF ERA-Interim global reanalysis (Dee et al., 2011), and these initial conditions and atmospheric state are adjusted by the model adjoint to minimize the cost function. SOSE air-sea fluxes have been extensively validated and shown to reduce biases in reanalysis flux products (Cerovečki et al., 2011).

Subgrid-scale parameterizations are employed to represent small-scale mixing processes, with coefficients typical of those used in eddy-permitting models. The horizontal biharmonic diffusivity parameterization ($10^{10} \text{ m}^4 \text{ s}^{-1}$) is employed to represent the unresolved subgrid scale mixing (Mazloff et al., 2010). There is no isopycnal mixing parameterization in SOSE. Rather, the resolved eddies themselves, obeying dynamical constraints, naturally stir along isopycnals. The small-scale tracer variance generated by this isopycnal stirring is dissipated by a combination of vertical, horizontal, and numerical mixing. The K-profile parameterization (KPP) scheme (Large et al., 1994) is employed to represent unresolved mixing processes, and below this the diffusivity decays to a constant background vertical diffusivity ($10^{-5} \text{ m}^2 \text{ s}^{-1}$) in the interior below the KPP boundary layer.

Although SOSE includes no additional parameterizations besides a constant background diffusivity below the KPP boundary layer, mixing arises due to constant vertical mixing or cabbeling or thermobaricity that result from a combination of eddy mixing and nonlinearities in the equation of state. Thus, density changes in the ocean interior can be enhanced by strong gradients generated by mesoscale eddy activity. SOSE does not adequately resolve bottom boundary layers due to low vertical resolution of the model grid in the deep ocean nor does it include internal lee wave parameterizations. Thus, there are diapycnal mixing processes in the abyssal ocean responsible for significant water mass transformation of Antarctic Bottom Water (AABW) that are not represented here (Nikurashin & Ferrari, 2013; Waterhouse et al., 2014). Therefore, we will focus only on the magnitude and spatial distribution of diapycnal changes in deep water density classes in the interior.

For this study, we use the SOSE iteration-100 solution, which has been extensively validated against observations (Abernathay et al., 2016; Tamsitt et al., 2016, 2017), and spans 6 years (2005–2010).

2.2. Lagrangian Experiment and Analysis

The Lagrangian particle release experiment was run offline with the SOSE daily velocity output, using Octopus (<https://github.com/jinbow/Octopus>; Tamsitt et al., 2017). The particle tracking model uses a fourth-order Runge-Kutta scheme in time, and the trilinear interpolation scheme in space to retrieve particle velocity from the surrounding eight gridded SOSE velocity points. Particles are integrated with the deterministic SOSE daily-averaged velocities with a parameterization of diffusion for unresolved processes that are absent from the explicitly resolved velocity field. The diffusion is modeled by a random walk scheme, as described in Tamsitt et al. (2017), with a horizontal diffusivity of $25 \text{ m}^2 \text{ s}^{-1}$ and a vertical diffusivity of $1 \times 10^{-5} \text{ m}^2 \text{ s}^{-1}$. The model implements a reflective boundary condition at the surface and bottom. When particles are within the ML, a random reshuffle of the vertical position of the particle within the ML is included every 5 days to represent ML turbulence that is not explicitly resolved in the SOSE velocities (Tamsitt et al., 2017). The majority of this analysis will focus on the particle trajectories prior to first entering the ML, so will not be significantly affected by the ML parameterization.

A total of more than 2.5 million particles were released at 30°S in the 1,000–3,500 m depth range in each ocean basin at each grid point (14 vertical levels in SOSE), spanning the σ_2 density range $36.2\text{--}37.1 \text{ kg m}^{-3}$, similar to that described in Tamsitt et al. (2017). Particles were rereleased at the same location every 30 days for the 6 years of SOSE daily-averaged output, and trajectories were integrated for 200 years, looping the model velocity output similar to a previous Lagrangian particle release experiment using SOSE (Van

Sebille et al., 2013). Small model drifts can cause unphysical jumps in density at the looping time step. To prevent this causing artificial changes in density along trajectories, the vertical position of particles is adjusted to conserve neutral density (γ_n) at the looping time step. Previous work looking at a deep pathway in the South Atlantic found that spatial pathways were insensitive to changes in the length of velocity output used (Van Sebille et al., 2012). However, in this case, with only 6 years of velocity output there may be temporal variability on decadal and longer time scales that is not captured. Longer velocity output is currently unavailable, but in the future further investigation into the importance of longer time scale velocity variability on the results would be valuable.

Similar to Tamsitt et al. (2017), we select the subset of particles with initial southward velocities at 30°S that remain south of 30°S and reach the ML during the 200 year experiment as representing the upwelling branch of the Southern Ocean overturning circulation. There are several reasons for rejecting particles that go north of 30°S: (1) because we rerelease particles at 30°S every month for the first 6 years, the pathways of particles that go north and return back south are represented, provided that they remain within the range of depths as the release; (2) this isolates transformation happening to deep water particles only south of 30°S; and (3) SOSE has a northern boundary at 25°S where particles can leave the northern boundary so we cannot account for the particles that exit this boundary. The resulting analysis includes 87,000 particle trajectories, less than 5% of the original >2.5 million particles released. This small fraction arises mostly because of very broad initial conditions, and we are confident that the sample adequately represents the vast majority of the Southern Ocean upwelling and have accounted for the destination of the remaining particles. Breaking down the fate of all of the particles: at the release, 44% of the particles have initial southward velocities in the depth layers we are interested in (the velocities are split almost equally northward and southward and we had initially seeded over a slightly broader depth range). Considering only those that do go south initially, 75% of these cross north of 30°S at some stage and do not upwell within 200 years, 15% go north of 30°S at some point before returning south and upwelling in the Southern Ocean, and 2.5% remain south of the 30°S and never upwell. The remaining 7.5% stay south of 30°S and upwell within 200 years, which are the particles analyzed here. The fate of the 2.5% that remain unaccounted for in the Southern Ocean without upwelling is of interest, and we have quantified that 10% of these remaining particles entered the AABW density class without upwelling.

In Tamsitt et al. (2017), the authors “tagged” particles with volume transport at the release location to track the relative transport carried by particles between 30°S and the mixed layer. With this tagging method, the total transport of the upwelled particles using the same criteria as this analysis in SOSE is 21.3 Sv, compared to 29 Sv in the southward limb of the overturning streamfunction in SOSE. We note that the two estimates are not expected to agree exactly as we only select particle trajectories that reach the mixed layer, while in the overturning streamfunction, there is a portion of the southward upwelling limb that is entrained into either intermediate or abyssal waters in the interior without ever reaching the mixed layer. Additionally, there is likely a small fraction of Lagrangian particle-transport that takes longer than 200 years to upwell and thus is not captured in our total transport. The upwelling pathways in SOSE were shown to agree well with two 1/10° resolution models, and all three showed similar topographic hot spots of upwelling (Tamsitt et al., 2017).

The time scale for particles to upwell from 30°S to the ML in SOSE is approximately 60–90 years, although these time scales are faster in the 1/10° models. It is likely that a “tail” of upwelling particles that take longer than 200 years to upwell is not captured, as shown in the shapes of the transit time distributions (Tamsitt et al., 2017, Figure 4). As a result, slower upwelling pathways (e.g., from the Pacific Ocean) may be underrepresented in our results. The ML was defined in SOSE at each location and time using the second derivative of density to find the inflection point at which $\partial\rho/\partial z$ switches sign. This method was chosen because it gives reasonable estimates over a broad range of regions, where threshold methods may not perform well in poorly stratified regions such as the Weddell and Ross Seas (Holte & Talley, 2009). We note this mixed layer depth definition differs slightly from the KPP boundary layer depth, which is defined using a bulk Richardson number criterion and means that the depth at which the KPP scheme has enhanced vertical diffusivities may differ somewhat from the mixed layer depth.

The potential temperature, salinity (PSU) are recorded following each individual trajectory, from which we calculate the potential density referenced to 2,000 m (σ_2) using the TEOS-10 nonlinear equation of state (McDougall & Barker, 2011). σ_2 is chosen as the 2,000 m reference density, reflecting the mean depth of the

initial particle release locations. We choose to analyze σ_2 rather than γ_n because σ_2 is a quasi-material variable, that is, it changes only as a result of irreversible mixing processes, while γ_n is not (McDougall & Barker, 2011; McDougall & Jackett, 2005). Additionally, there are technical difficulties that make it very challenging to calculate the Eulerian water mass transformation rate in γ_n online in SOSE (see section 2.3). We recognize that there are disadvantages to using σ_2 , particularly the fact that thermobaric effects are not included in the analysis in σ_2 , that are captured by calculating water mass transformation in γ_n . Thermobaric effects are strong in the Southern Ocean because of steep isopycnal slopes and large isopycnal temperature gradients (Groeskamp et al., 2016; Klocker & McDougall, 2010; Stewart & Haine, 2016). Thus, to show that our results are not qualitatively influenced by the choice of density coordinate, we show the overall Lagrangian water mass transformation in both σ_2 and γ_n but present the rest of the analysis in σ_2 in order to compare with Eulerian water mass transformation in SOSE (section 3.3).

The majority of particles cross into the ML at depths in the upper 100–200 m, but there is a long tail of particles that upwell across deep winter MLs (Figure 2a). The SOSE solution has a deep convection event in the Weddell Sea in 2005 (which did not occur in ocean observations), leading to MLs deeper than 1,000 m, but these influence only a small fraction of particles. It has been demonstrated that the instantaneous ML is not a good boundary to separate the region of the ocean with large diapycnal changes due to surface processes from the interior, and that significant water mass transformation occurs just below the ML (Iudicone et al., 2008b). Therefore, to separate particles in the interior from particles exposed to surface heat and freshwater fluxes, we define the “surface diabatic layer” (SDL) as the maximum σ_2 at each latitude and longitude that outcrops at least once during the 6 year SOSE iteration (Figure 2; Cervenécká & Marshall, 2008). This essentially separates isopycnal layers that “feel” the surface at some time during the 6 years from those that are never exposed to surface fluxes. This is similar to the “mixed layer bowl” concept used by Marshall et al. (1999) and Iudicone et al. (2008a), which identifies the maximum ML depth at each location.

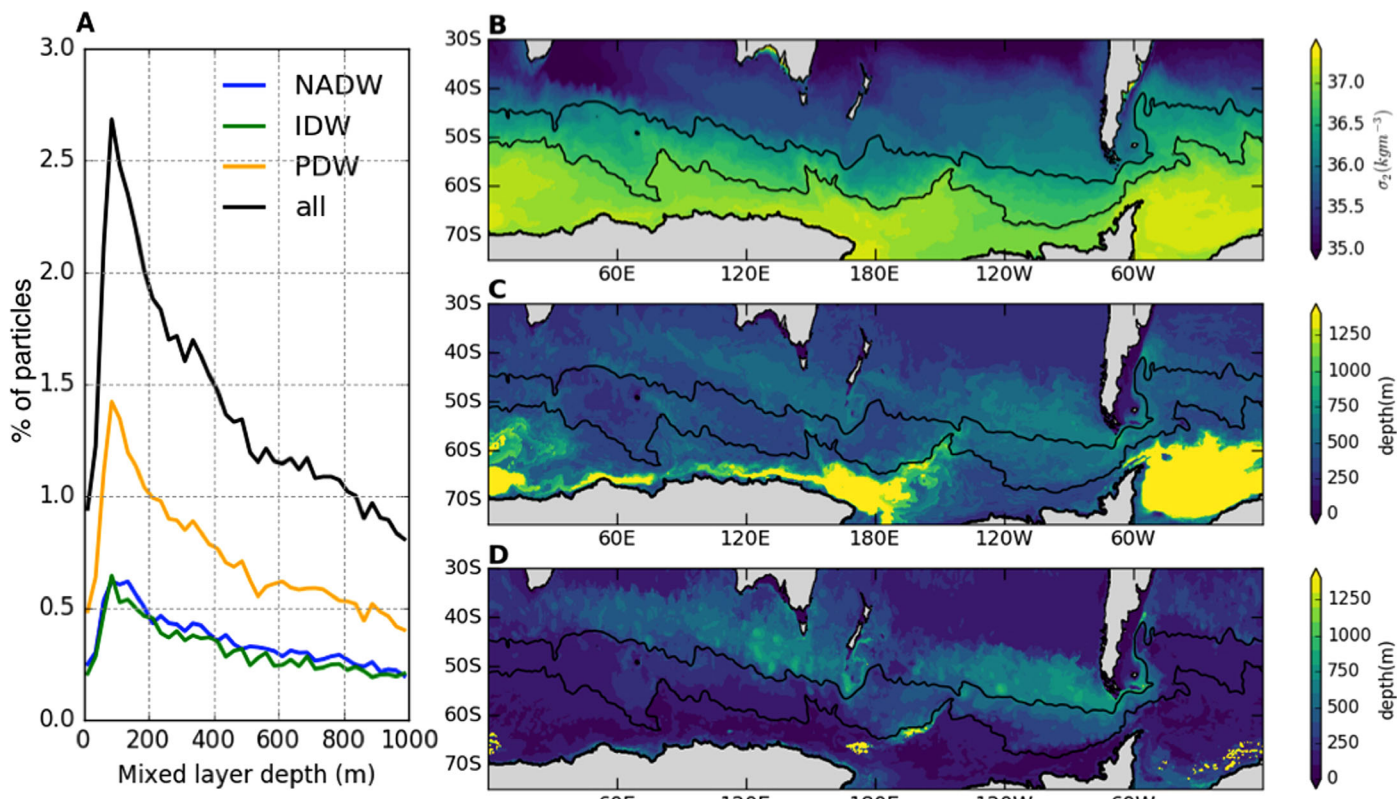


Figure 2. (a) Distribution of depth of mixed layer at particle first crossings, (b) σ_2 of the surface diabatic layer (SDL) at each grid point, (c) mean depth of the SDL σ_2 at each grid point, and (d) depth of the mixed layer “bowl,” which is the maximum mixed layer depth at each grid point for the 6 year period.

We wish to clarify the language used to describe water mass transformation in this analysis. A process is considered “adiabatic” if it occurs without exchange of heat and also without the internal dissipation of kinetic energy (McDougall & Barker, 2011). In the literature, the word “adiabatic” is often used to refer to a circulation that occurs without modifying the buoyancy of seawater. This usage is correct in idealized models that consider only temperature and not salinity (e.g., Nikurashin & Vallis, 2011; Wolfe & Cessi, 2011). However, when salinity is present, it is more accurate to describe a circulation pathway as “isopycnal” when the buoyancy remains constant and “diapycnal” when it is not. We strive to use these terms correctly, making exceptions in cases of established terminology, such as the “surface diabatic layer” (Cerovečki & Marshall, 2008), which refers to the upper ocean layer that is exposed to surface forcing.

The SDL in SOSE shows very dense waters, with $\sigma_2 > 37.1 \text{ kg m}^{-3}$, outcropping south of the ACC at some time during the 6 year iteration (Figure 2b). The mean SDL depth exceeds 1,000 m in the Weddell and the western Ross Seas, due to inversions in the σ_2 profile in these regions (Figure 2c). Outside of these two regions, the SDL depth is similar to the “mixed layer bowl,” and the results following are qualitatively similar using a “mixed layer bowl” rather than the SDL (not shown) (Figure 2d). Particles take a median of 79 years, with a standard deviation of 42 years, to travel from 30°S to first crossing of the SDL, compared to a median of 17 years (25 years standard deviation) to travel between first crossing of the SDL and crossing the ML. Thus, an average particle spends approximately 1/5 of its total upwelling time traveling between the SDL and the ML.

It is worth noting that with background diffusion, we should not view any single particle trajectory as a “pathway” but view water mass pathways as a statistical quantity from an ensemble of particles. It is useful to define the probability density function based on a large group of particles, which can be used to calculate the first and higher order moments to gain more insight into the process of the water mass transformation. The probability density function (PDF) in this Lagrangian method is simply defined as the normalized particle distribution within any variable space tagged along the particle trajectories, such as density, temperature, salinity or eddy kinetic energy. It is numerically calculated by binning particles and counting the particle numbers in each bin. We denote the property χ of the i th particle as χ^i . The particle PDF in χ space is written as

$$P(\chi) = \frac{1}{N} \sum_{i=1}^N \xi_i, \\ \xi_i = \begin{cases} 1, & \text{if } \chi - \delta/2 < \chi^i \leq \chi + \delta/2 \\ 0, & \text{else} \end{cases}, \quad (1)$$

where N is the total number of particles, and δ is the bin width. In the following, we will replace χ with density, potential temperature, salinity, and eddy kinetic energy to examine the Southern Ocean upwelling pathways from different perspectives.

2.3. Eulerian Water Mass Transformation Analysis

A useful complementary analysis to the Lagrangian experiments is to directly calculate Eulerian water mass transformation in SOSE, which will be compared and contrasted with the Lagrangian results in section 3.3. Water mass transformation quantifies the rate at which water masses change their properties due to irreversible thermodynamic processes (mixing and boundary fluxes). Here we consider water mass transformation in σ_2 potential density coordinates (Marshall et al., 1999). In a steady state, the net water mass transformation within an ocean basin must match the volume inflow/outflow at the basin boundary (Walsh, 1982). Because of this conservation property, water mass transformation rates are usually presented as integrals over whole basins. However, it is also possible to calculate a transformation map, which describes the rate of water mass change at each point in space (e.g., Brambilla et al., 2008). This “local” transformation rate is equivalent to the diapycnal velocity in thickness-weighted isopycnal coordinates (Young, 2012).

The potential density equation is

$$\frac{D\sigma_2}{Dt} = \dot{\sigma}_2 = \frac{\partial\sigma_2}{\partial\theta} \dot{\theta} + \frac{\partial\sigma_2}{\partial S} \dot{S}, \quad (2)$$

where $\dot{\theta}$ and \dot{S} represent all nonadvective sources (i.e., external forcing and mixing) of potential temperature (θ) in degrees Celsius and salinity (S) in PSU, respectively. The partial derivatives $\partial\sigma_2/\partial\theta$ and $\partial\sigma_2/\partial S$

are related to thermal expansion and haline contraction and are evaluated from the model's thermodynamic equation of state (Jackett & McDougall, 1995). The local transformation rate is defined as

$$\omega(x, y, \sigma_2, t) = \frac{\partial}{\partial \sigma_2} \overline{\int_{\sigma'_2 < \sigma_2} \dot{\sigma}_2 dz}, \quad (3)$$

where the overbar indicates a time average (here over the 6 year SOSE integration interval) and the integration is performed in the vertical up to the target isopycnal depth. ω has units of $m s^{-1}$.

This expression is evaluated numerically by discretizing σ_2 into 400 unevenly spaced bins. The bin spacing $\Delta\sigma_2$ varies from 0.025 kg m^{-3} at low density to 0.0025 kg m^{-3} at high density. This spacing was chosen to provide good resolution of the high-density polar water masses, which occupy a relatively small segment of the density range but with a large depth range. Within each bin, (3) is evaluated numerically as

$$\omega(x, y, \sigma_2, t) = \frac{1}{\Delta\sigma_2} \sum_{k=1}^{N_z} \dot{\sigma}_2 h_c \Delta z_f \delta(\sigma_2 - \sigma'_2), \quad (4)$$

where h_c is the partial grid cell fraction (Adcroft et al., 1997), and Δz_f is the height of the tracer grid cell, and N_z is the number of vertical grid cells. The function $\delta(\sigma_2 - \sigma'_2)$ is a numerical delta function, defined as

$$\delta(\sigma_2 - \sigma'_2) = \begin{cases} 1 & \text{if } (\sigma_2 - \Delta\sigma_2/2) \leq \sigma'_2 < (\sigma_2 + \Delta\sigma_2/2) \\ 0 & \text{else} \end{cases}. \quad (5)$$

The time averaging in (4) is performed "online," i.e., at every time step as the model is running, using the MITgcm LAYERS package. (The highest possible temporal resolution is required for accurate calculation of water mass budgets (Ballarotta et al., 2013; Bryan & Bachman, 2015; Cerovecki & Marshall, 2008).) The nonadvective potential density tendency $\dot{\sigma}_2$ is the sum of six individual subcomponents corresponding to surface forcing, vertical mixing (including the KPP parameterization), and horizontal mixing for both potential temperature and salinity, enabling a detailed decomposition of the thermodynamic processes that drive changes in water mass density.

Over a very short interval, ω should in principle be equal to the rate with which Lagrangian particles move across isopycnal surfaces. This equivalence breaks down, however, for long averaging times and when only a subset of particles is analyzed (as is the case for the upwelling particles examined here). Nevertheless, comparing Lagrangian density changes to Eulerian water mass transformation maps helps understand the thermodynamic drivers of the density changes (e.g., mixing versus surface forcing).

3. Results

3.1. Lagrangian Water Mass Transformation

It is instructive to take a probabilistic approach to cumulative density changes along particle trajectories, thus showing the likelihood of a deep water particle falling within a range of densities using particle PDFs as defined in equation (1). With this tool we can quantify the probability that a water parcel from the deep ocean will upwell along isopycnals, and the likelihood that its density will increase or decrease. We define the density anomaly, $\Delta\sigma_2$ (in units of kg m^{-3}), as the difference between density at a given point in time and the initial density at the release location at 30°S . $\Delta\sigma_2$ represents the cumulative, or net, density change between release and a given location and time, and thus density increases and decreases can occur in between that are compensated, leading to no net density change. We note that as particles get closer to the sea surface, particularly as they travel between the SDL and ML, the $\Delta\sigma_2$ values misrepresent the actual diapycnal density change, as the σ_2 coordinate drifts further from the true isopycnal surface toward the sea surface. (Particles that become lighter in σ_2 are actually becoming even more buoyant, as seen by the rotation of σ_θ contours relative to σ_2 contours.) We bin the density and density anomaly in 0.1 kg m^{-3} bins to obtain the sample PDF. In Figure 3, we show the PDFs of density and density anomaly at the particle release location, first crossing of the SDL and first crossing of the ML, with the contributions from particles originating in the Atlantic, Indian and Pacific to the total PDF shown individually (Figure 3).

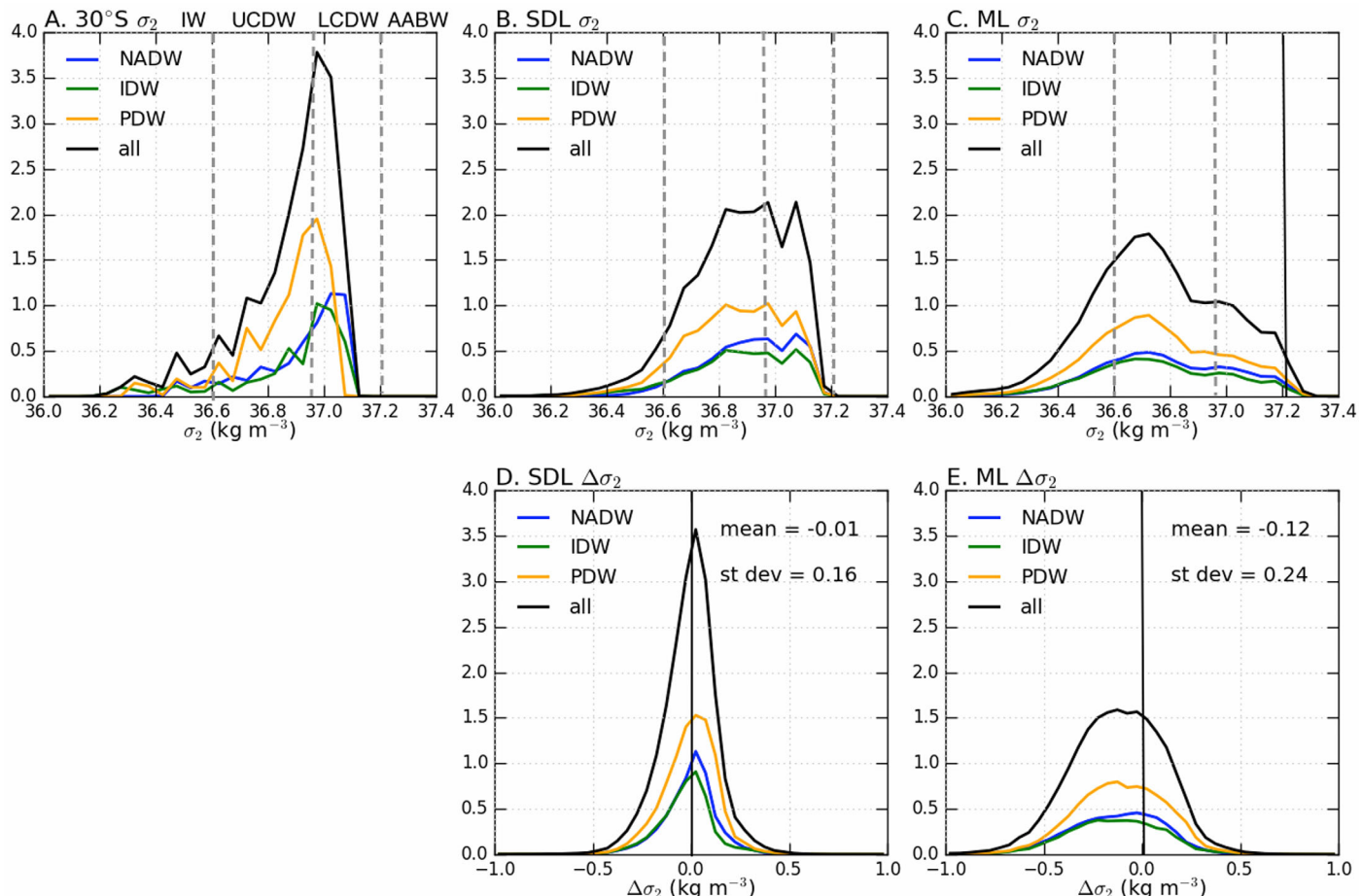


Figure 3. Probability density functions of all particles (black) and the contributions to the total PDF from the Atlantic, Indian and Pacific basins (colors) for (a) σ_2 at release location at 30°S, (b) σ_2 at first crossing of the SDL, (c) σ_2 at first ML crossing, (d) $\Delta\sigma_2$ at first crossing of the SDL, and (e) $\Delta\sigma_2$ at first ML crossing. Dashed lines in Figures 3a–3c indicate the boundaries between different water masses listed in Table 1 and the solid vertical lines in Figures 3d and 1e indicate 0 $\Delta\sigma_2$, or no density change. The mean and standard deviation of $\Delta\sigma_2$ are shown in Figures 3d and 3e.

The distribution of density at the particle release locations (Figure 3a) is broad but unevenly distributed in σ_2 space. Because the particles are released in an even distribution in depth space at 30°S, they are unevenly distributed in density space and the chosen subset of particles that eventually reach the ML furthers the uneven sampling in density space. In this case, we have chosen to distribute evenly in depth space as this more accurately represents the total volume of upwelling deep water and thus density classes with larger volume have a larger contribution to the bulk density statistics. As is clear in Figure 3a, our analysis includes a broad range of densities, so to further understand the changes in density during upwelling, we define separate water masses within this range. Using the same water mass definitions as used to analyze the same iteration of SOSE in Abernathey et al. (2016) (following Speer et al. (2000) and Downes et al. (2011)), we define four water masses: Intermediate Waters (IW), Upper Circumpolar Deep Water (UCDW) and Lower Circumpolar Deep Water (LCDW), and Antarctic Bottom Water (AABW) (Table 1). The results are not sensitive to the exact water mass definitions. We also note that we refer to deep water originating in each ocean as North Atlantic Deep Water (NADW), Indian Deep Water (IDW), and Pacific deep water (PDW), but for this analysis these definitions refer only to the basin of origin and not a particular density range.

At 30°S, the mode in the PDF of σ_2 is 36.9 kg m^{-3} and the distribution is skewed toward lighter densities, with a sharp drop off in the probability of particles being denser than 36.9 kg m^{-3} and a broad tail of lighter particles. The particles are divided with 8.3% initially in the IW density range, and the remaining split almost equally between the UCDW and LCDW density classes. The distributions of σ_2 in each basin show that upwelling particles originating in the Pacific dominate the total number of upwelling particles, and more Pacific particles originate at lighter densities than those originating in the Atlantic and Indian Oceans.

Table 1

Water Mass Definitions, Showing the Neutral Density (γ_n) Range Used in the Same Iteration of SOSE in Abernathey et al. (2016), and the Equivalent σ_2 Ranges for Upwelling Water in This Study

Water mass	γ_n (kg m ⁻³)	σ_2 (kg m ⁻³)	% at release	% at SDL	% at ML
IW	27.0–27.5	<36.6	8.3	7.2	25.8
UCDW	27.5–28.0	36.6–36.95	46.6	55.3	50.7
LCDW	28.0–28.2	36.95–37.2	45.1	37.5	21.4
AABW	>28.2	>37.2	<0.1	<0.1	2.1

Note. The rightmost three columns show the percentage of total upwelling particles in each density class at the particle release location at 30°S, at the first crossing of the SDL and at the first crossing of the ML.

When particles first cross the SDL, the distribution of particle σ_2 has become more evenly distributed, with fewer particles occupying the lightest density classes, and a broadened peak encompassing dense UCDW and light LCDW (Figure 3b). The distribution of $\Delta\sigma_2$ at the time when particles cross the SDL for the first time is symmetric and centered close to zero (i.e., no net density change), with a mean $\Delta\sigma_2$ of -0.01 kg m⁻³ and a standard deviation of 0.16 kg m⁻³ (Figure 3d). Thus, the net diapycnal transformation in the ocean interior prior to reaching the SDL is small, mostly characterized by a spread of the PDF to both higher and lower densities rather than a shift in the mean. We note that the the small total mean density decrease below the SDL is mostly due to particles originating in the Atlantic and Indian, with mean $\Delta\sigma_2$ of -0.01 and -0.03 kg m⁻³, respectively, while the mean Pacific $\Delta\sigma_2$ is negligible.

In contrast, when particles reach the ML for the first time, the distribution of σ_2 of particles from all origins has changed significantly, with 68% of particles lighter than at their initial density at release. There is a broad tail at higher densities, including 2.1% of particles denser than 37.2 kg m⁻³, which have mixed with denser waters to enter the AABW density class prior to reaching the ML (Figure 3 and Table 1). We note that this 2.1% of particles only captures particles converted to AABW that upwell to the mixed layer and thus does not represent the full conversion of deep waters to AABW, as there is likely a subset of particles converted to AABW that never reach the mixed layer. At the ML crossing, the PDF of $\Delta\sigma_2$ remains symmetric, but the distribution is shifted toward substantially lighter densities, with a mean density anomaly of -0.12 kg m⁻³ and standard deviation of 0.24 kg m⁻³. This distribution is similar for all three basins of origin. This shows that between the SDL and ML, particles undergo much larger net density changes relative to changes before crossing the SDL, with a strong bias toward lighter densities. This result justifies the use of SDL as a definition for separating the interior ocean, where the upwelling is relatively isopycnal and transformation results from mixing, from the upper ocean where surface forcing also contributes resulting in a much larger net density change.

Figure 4 shows the same PDFs as Figure 3 but calculated using γ_n as the density coordinate rather than 3. The distributions of density and density anomaly are very similar, indicating that our conclusions are not particularly sensitive to the choice of density coordinate. In particular, the $\Delta\sigma_2$ and $\Delta\gamma_n$ at the SDL crossing (Figures 3d and 4d) are almost identical, with the same mean and very similar standard deviations (0.16 for $\Delta\sigma_2$ and 0.14 for $\Delta\gamma_n$). Above the SDL, where there are larger differences between σ_2 and γ_n surfaces, the density change is generally larger in γ_n than σ_2 . The mean of $\Delta\gamma_n$ at the ML crossing are -0.26 kg m⁻³, more than double that of $\Delta\sigma_2$ (-0.12 kg m⁻³) and the standard deviation of $\Delta\gamma_n$ (0.76 kg m⁻³) is three times that of $\Delta\sigma_2$ (0.24 kg m⁻³). The result that density decreases more in γ_n is somewhat surprising, as previous water mass transformation analyses indicate that thermobaricity (which is captured in γ_n but not σ_2) increases density in deep waters in the Southern Ocean (Groeskamp et al., 2017). This may be due to the fact that density change in σ_2 is an underestimate of the actual density change as particles venture further from the 2,000 db reference pressure as they approach the sea surface (see section 3.3).

Given the wide range of initial densities captured in Figure 3a, it is useful to look at the evolution of particle densities as a function of initial density as differing transformation of individual density classes may be obscured in the bulk PDFs in Figure 3. Figure 5a shows a joint PDF of particle initial release density and density at the SDL crossing, with values above the 1:1 line indicating a net density increase and below the 1:1 line indicating a net density decrease. These changes result from mixing, which can cause density to increase or decrease, or from cabling, which only increases density, or thermobaricity, which can increase

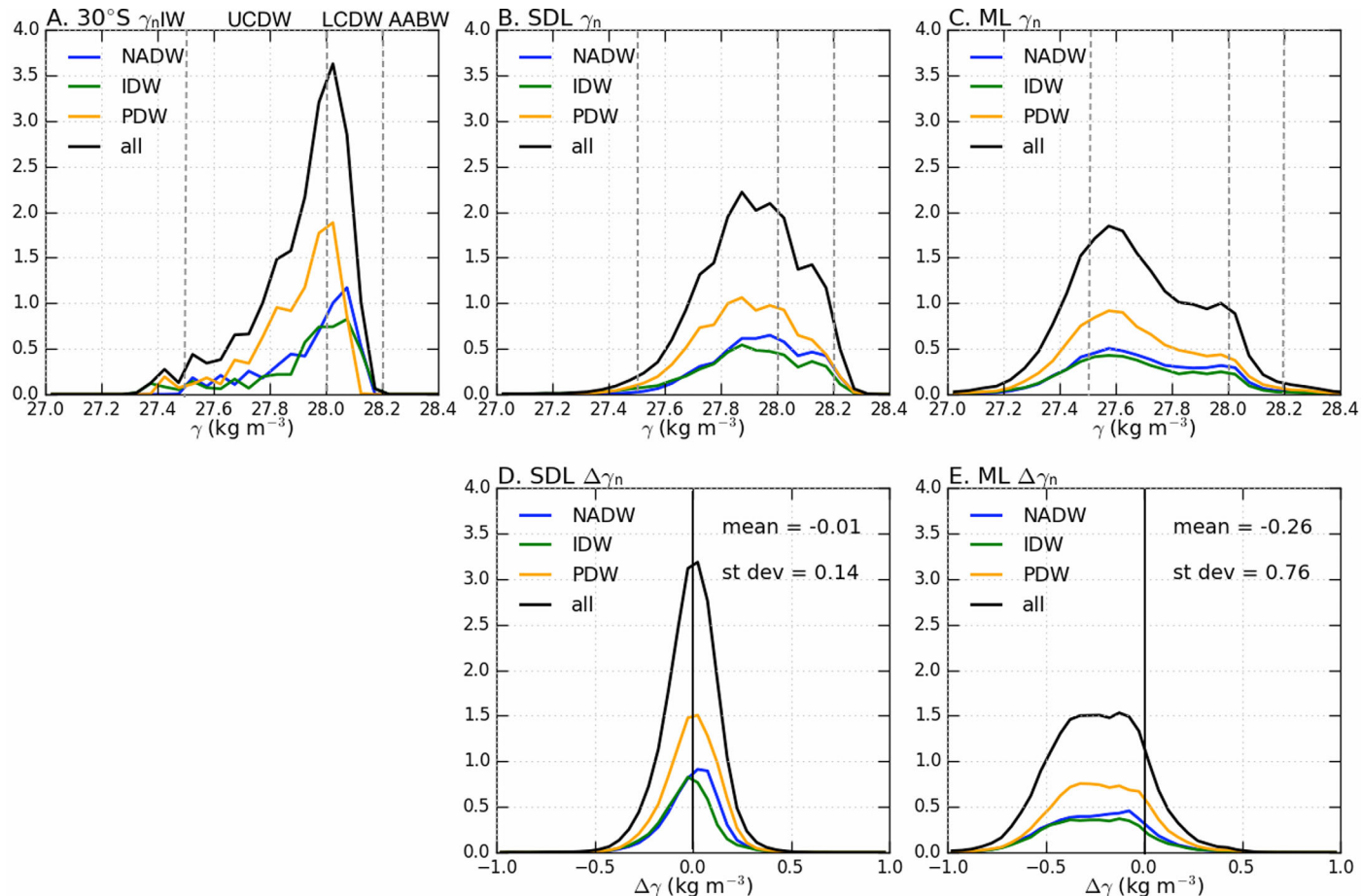


Figure 4. Probability density functions of all particles (black) and the contributions to the total PDF from the Atlantic, Indian and Pacific basins (colors) for (a) γ_n at release location at 30°S , (b) γ_n at first crossing of the SDL, (c) γ_n at first ML crossing, (d) $\Delta\gamma_n$ at first crossing of the SDL, and (e) $\Delta\gamma_n$ at first ML crossing. Dashed lines in Figures 4a–4c indicate the boundaries between different water masses listed in Table 1 and the solid vertical lines in Figures 4d and 4e indicate $0 \Delta\gamma_n$, or no density change. The mean and standard deviation of $\Delta\gamma_n$ are shown in Figures 4d and 4e.

or decrease density. The lightest waters (IW density class) show a distinct shift toward the denser UCDW density class, while particles originating in the UCDW density class with $\sigma_2 > 36.8 \text{ kg m}^{-3}$ shift toward lighter densities during upwelling, leading to a convergence of these two water masses. This density convergence may result from mixing of different source deep waters as they interact in the ACC. The small net lightening of the UCDW implies that the mixing processes making them lighter are more vigorous than cabbeling. In contrast, the particles originating in the densest LCDW tend to become denser during upwelling, with a very small fraction reaching AABW densities by the time they cross the SDL. Cabbeling may contribute significantly to this densification of LCDW, as observations suggest that there is significant formation of dense LCDW and AABW by cabbeling in the Southern Ocean (Foster, 1972; Groeskamp et al., 2016).

The buoyancy gain of UCDW particles and buoyancy loss of the densest LCDW particles results in divergence toward two separate water masses in the ocean interior, as is visible in the two peaked structure in Figure 3b. This transformation of deep water toward lighter IW and denser AABW in the ocean interior prior to reaching the mixed layer has been shown in previous model analysis (Judicone et al., 2008a). We note that because we consider only particles that upwell to the ML, there is likely a subset of deep water particles entrained into AABW that never outcrop into the mixed layer and thus are not captured in this Lagrangian analysis.

After crossing the SDL, but before reaching the ML, a strong shift toward lighter densities is clear for all particles apart from those crossing the SDL at densities greater than $\sigma_2 = 37.0 \text{ kg m}^{-3}$. These densest waters show similar likelihoods of increasing or decreasing density before reaching the ML, causing further

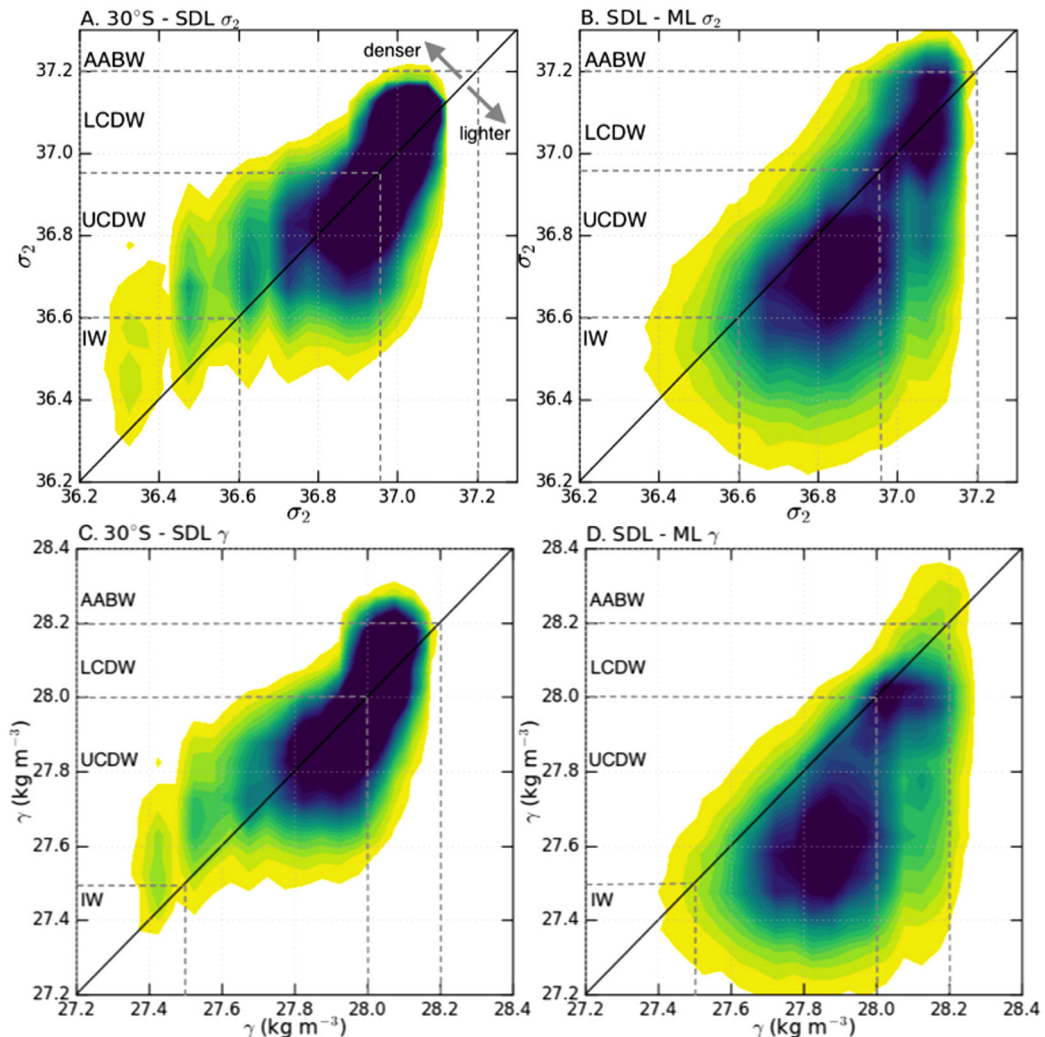


Figure 5. Joint probability density function of (a) σ_2 at release location at 30°S compared to σ_2 at first crossing of the SDL, (b) σ_2 at first crossing of the SDL compared to σ_2 at first crossing of the ML, (c) same as Figure 5a for γ_n , and (d) same as Figure 5b but for γ_n . The solid 1:1 line in each figure indicates no density difference, values above the line indicate a density increase, and below the line indicate a density decrease. Dashed lines indicate the boundaries between different water masses in σ_2 and γ_n listed in Table 1.

divergence of the densest waters from the bulk of particles reaching the ML as UCDW. Our analysis shows that while upwelling in the interior below the SDL is relatively isopycnal, the upwelling deep water experiences large diapycnal changes before crossing the ML, is significantly modified by mixing, and is influenced by surface heat and freshwater fluxes. This is consistent with previous work that finds substantial water mass transformation below the ML (Iudicone et al., 2008a). Again we compare the density anomaly in σ_2 (Figures 5a and 5b) to γ_n (Figures 5c and 5d) and find the results are qualitatively very similar, but there are larger density decreases between the SDL and ML when calculated in γ_n relative to σ_2 similar to (Figure 4). To aid in the comparison with Eulerian water mass transformation in SOSE, for the remainder of the analysis we will show the lagrangian transformation using σ_2 as the density coordinate.

Our results suggest that some of the deep water originating in the Atlantic and Indian that is initially in the LCDW density range is converted to the UCDW density range prior to reaching the mixed layer (Figures 3a and 3b), resulting in distributions of densities at the SDL crossing that are more similar to the Pacific deep water distribution (which is essentially unchanged). We find that the transformation of deep water between 30°S and reaching the northern ACC boundary differs by basin (not shown), but once particles enter the ACC and eventually cross the SDL, the density distributions are much more similar, but retain small mean

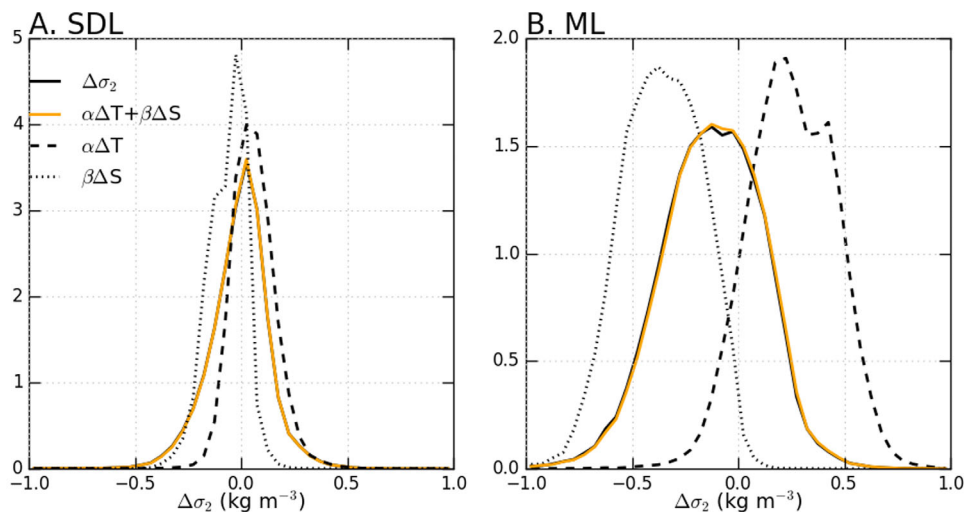


Figure 6. Probability distribution function of particle $\Delta\sigma_2$ and contributions from $\Delta\theta$ and ΔS at (a) first crossing of the SDL and (b) first crossing of the ML. Note that the y-axis limits differ in Figures 6a and 6b.

density differences, as will be shown in more detail in the next section. Very few particles analyzed here that upwell all the way to the mixed layer are transformed to AABW before crossing the SDL. However, it is important to note that transformation of Deep Waters to AABW may take place largely below the mixed layer and in polynyas; particles that transform from Deep Water to AABW without entering the mixed layer are not represented in our analysis. Moreover, the AABW production rate appears to be significantly underestimated in SOSE compared with observed transports, as reported in many papers and summarized in Talley (2013). Further analysis in upcoming years with models of increased spatial resolution and more realistic polynya representation will be of great interest in this regard.

3.2. Changes in Temperature and Salinity

We further decompose the density change along trajectories into separate contributions from temperature and salinity, using the relationship $\Delta\sigma_2 = -\alpha(\theta, S)\Delta\theta + \beta(\theta, S)\Delta S$, where θ is potential temperature, S is salinity, α is the thermal expansion coefficient, and β is the haline contraction coefficient (both coefficients calculated at a pressure of 2,000 db). We note that this decomposition would not be possible with neutral density without the addition of a constant factor that depends on space (Iudicone et al., 2008c). Similar to Iudicone et al. (2008a), we approximate this using an integral approach as $\Delta\sigma_2 \approx -\bar{\alpha}(\bar{\theta}, \bar{S})\Delta\theta + \bar{\beta}(\bar{\theta}, \bar{S})\Delta S$, where the overbar is the average of the initial and final values. The sum of the temperature and salinity contributions to $\Delta\sigma_2$ derived in this way agrees closely with the total density change (Figure 6).

At the SDL crossing, there is strong compensation between temperature and salinity changes, but with a large overlap in the $\Delta\theta$ and ΔS distributions. $\Delta\theta$ is shifted toward positive values, indicating mixing with colder water, while salinity is shifted toward negative values, indicating mixing with fresher water (Figure 6a). The colder and fresher water that mixes along isopycnals with the upwelling deep water likely originates as Antarctic Surface Water at the sea surface. At the ML crossing, there is less overlap in the $\Delta\theta$ and ΔS distributions and they are no longer density compensated, with the ΔS distribution centered further to the left (Figure 6a). Therefore, the shift in $\Delta\sigma_2$ toward lighter densities between the SDL and the ML is accomplished by decreasing salinity. In the same iteration of SOSE, Abernathey et al. (2016) found that vertical mixing of salt is the dominant contribution to the total water mass transformation in these same density classes due to mixing in the upper ocean, consistent with our Lagrangian result that ΔS causes the shift of σ_2 toward lighter densities above the SDL.

The distribution of particle densities can also be visualized in thermohaline coordinates (i.e., θ - S space), which can shed insight on the circulation beyond geographical coordinates (Döös et al., 2012; Groeskamp et al., 2014; Zika et al., 2012; Figure 7). This allows a clear distinction to be made between compensated changes in temperature and salinity due to isopycnal mixing and diapycnal mixing which leads to density

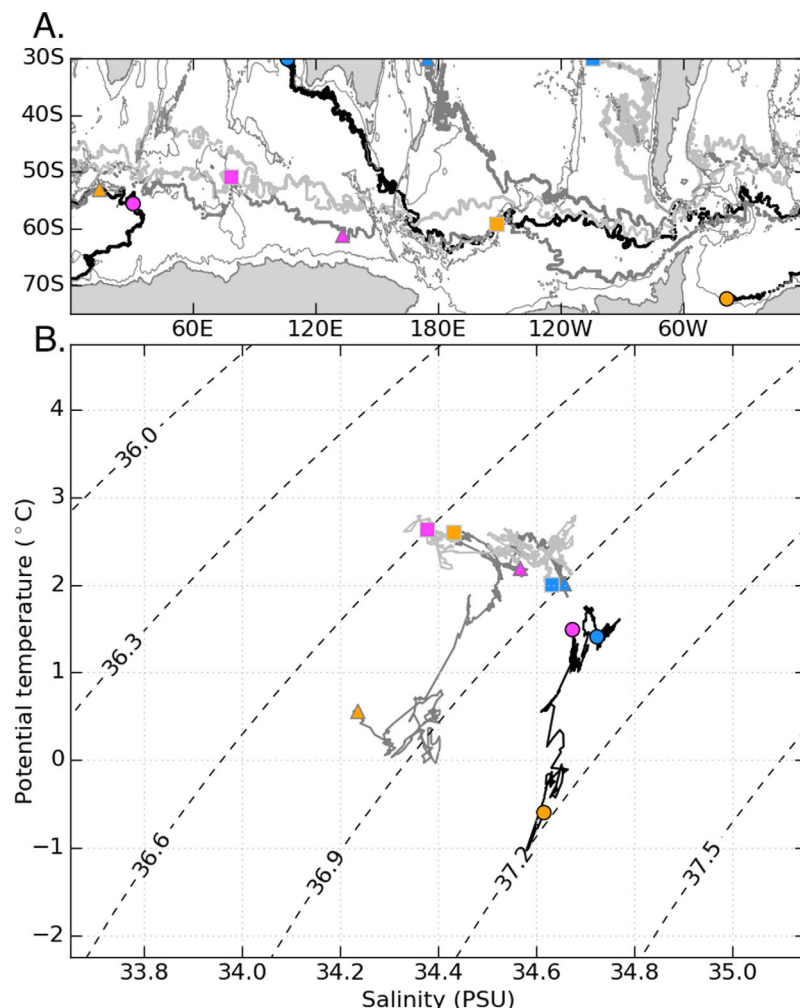


Figure 7. Lagrangian trajectories in θ -S space. (a) Map showing positions for three particles (black, dark grey, and light grey) with colored location at 30°S (blue), first crossing of the SDL (magenta), and first crossing of the ML (orange) and (b) same trajectories as Figure 7a but in θ -S space. Dashed black contours show σ_2 levels in θ -S space.

change. We note that changes in θ -S coordinates can occur both as a result of advection of a particle across temperature and salinity gradients, and due to local changes in temperature and salinity at a fixed location (Groeskamp et al., 2014). Figure 7 shows three examples of particle trajectories in θ -S space and their corresponding geographic locations, illustrating different pathways. Combining all upwelling trajectories, joint PDFs of particle θ and salinity in thermohaline coordinates at the release, SDL crossing, and ML crossing shows the progression of upwelling deep water from relatively warm and salty to colder and fresher at the SDL crossing and to three distinctly separate water masses at the ML crossing (Figure 8).

Between 30°S and the SDL, the core water mass properties of particles originating in the Atlantic show a predominantly isopycnal shift from the warm, salty signature of NADW toward colder, fresher waters (Figure 8a). In contrast, there is weaker modification of particles originating in the Indian (Figure 8b), and very little modification of deep water with Pacific origin (Figure 8c) below the SDL. The result is a convergence of water masses with different initial properties toward a single similar T-S distribution by the time particles reach the SDL (Figure 8d). Because the change in temperature and salinity is mostly density compensated even though well known (e.g., Sloyan & Rintoul, 2000), this transformation of NADW along density surfaces is often taken for granted, but was central to a global analysis of the ocean circulation in thermohaline coordinates (Zika et al., 2012). In addition to compensated change in properties, there is a very slight density decrease in Atlantic and Indian waters between 30°S and the SDL, as in Figure 3b.

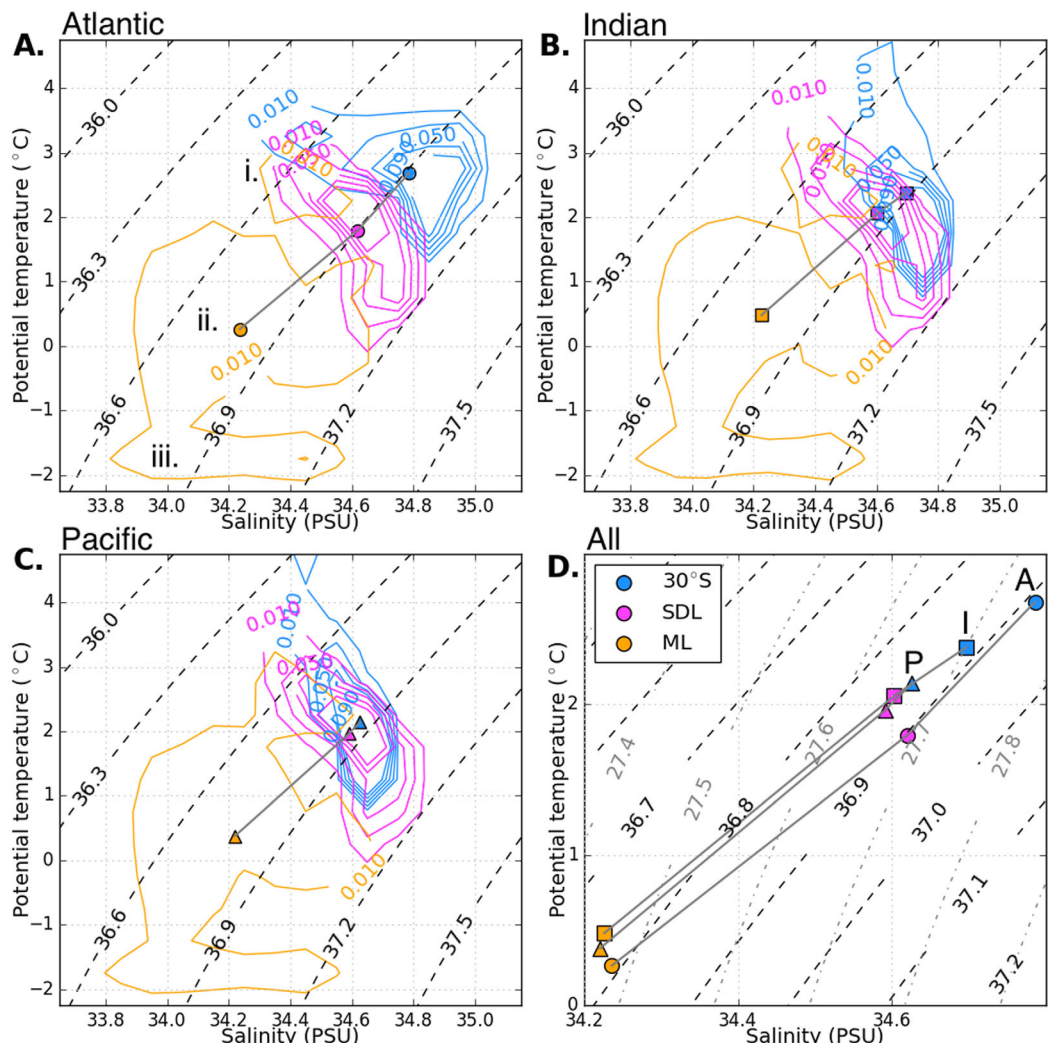


Figure 8. Joint probability distribution function of particle θ ($^{\circ}$ C) and salinity (PSU) at the release location (blue), SDL crossing (magenta), and ML crossing (orange) for (a) particles originating in the Atlantic, (b) Indian, and (c) Pacific. Dashed black contours show σ_2 levels in θ -S space. Blue, magenta, and orange filled shapes in each figure connected by grey lines show the progression of the mean particle θ -S properties at release, SDL crossing and ML crossing, respectively. (d) Zoomed in view of mean particle θ -S properties at release, SDL and ML for the Atlantic (A, circles), Indian (I, squares), and Pacific (P, triangles). Dashed black contours in each figure show σ_2 levels in θ -S space, and dash-dot grey contours in Figure 8d indicate σ_θ (potential density referenced to the sea surface) levels in θ -S space.

Between the SDL and ML, the θ -S properties diverge into three distinct water masses: a relatively warm, salty water mass of particles that upwell into the ML in subtropical western boundary currents (annotated as i. in Figure 8a); a broad, colder water mass spanning UCDW density classes (annotated as ii. in Figure 8a); and a separate water mass with close to freezing temperatures with the saltiest waters crossing into AABW densities (annotated as iii. in Figure 8a). As shown in Figure 5, this also indicates the divergence of water mass properties into two distinct branches prior to entering the ML and being exposed to direct surface buoyancy fluxes. It is also clear in Figure 8d that the center of mass of the density distribution of Atlantic deep water is initially slightly denser than Indian and Pacific deep waters. This mean density difference, albeit small, remains similar at 30° S, the SDL and ML, although the θ -S characteristics change substantially. Thus, although there is convergence of water masses in θ -S space in the interior and a large overlap in the density distribution of different deep waters, the difference in center of mass of the particle distribution between the Atlantic and Indo-Pacific deep waters is preserved during upwelling. This is consistent with the results of Talley (2013) and others that find the signature of deep waters of Atlantic origin is found at a higher density (and below) Indian and Pacific deep waters.

An important caveat that errors in our estimates of diapycnal change in σ_2 coordinates may be important in the upper ocean is clearly illustrated by the difference in slope of σ_2 and σ_0 contours in θ -S space shown in Figure 8d. The density change between the SDL (magenta) and ML (orange), where particles are in the upper ocean, is significantly larger in σ_0 than in σ_2 , suggesting that our $\Delta\sigma_2$ may be underestimating the true density change in the upper ocean.

3.3. Spatial Distribution of Transformation

It is clear from sections 3.1 and 3.2 that there are significant transformation along Lagrangian upwelling pathways in the interior of the Southern Ocean, but we take this a step further to look at where these processes occur spatially. Using the local density time rate of change along particle trajectories, $d\sigma_2/dt$, we bin the particle $d\sigma_2/dt$ in 1° latitude $\times 1^\circ$ longitude spatial bins for all particles at all times, and average all values in each bin to obtain an ensemble estimate of the density change rate at each location. Additionally, we separate the times at which particles are below the SDL and above the SDL, and bin average these separately to estimate the mean $d\sigma_2/dt$ in the ocean interior and the $d\sigma_2/dt$ above the SDL (Figure 9).

The maps of ensemble mean $d\sigma_2/dt$ in the interior and in the SDL show that, to first order, $d\sigma_2/dt$ along trajectories in the SDL is an order of magnitude larger than in the interior (Figure 9). In the interior, although $d\sigma_2/dt$ is relatively small, there is clearly enhanced ensemble mean $d\sigma_2/dt$ of similar magnitude to above the SDL in some locations, particularly in boundary currents, close to major topographic features and along the Antarctic coastline. Regions with high EKE (region within green contours in Figure 9a) encompass much of the enhanced interior $d\sigma_2/dt$ in boundary currents and near topography, but exclude enhanced transformation elsewhere, particularly along the Antarctic continental slope. The background transformation below the SDL is generally very weakly increasing density (positive transformation), but there are notable regions where particle density is decreasing (negative transformation). This includes the Agulhas Return Current and regions at major topographic features along the ACC, including the Kerguelen Plateau, Macquarie Ridge, Pacific-Antarctic Ridge and Drake Passage, where there are hotspots of negative transformation

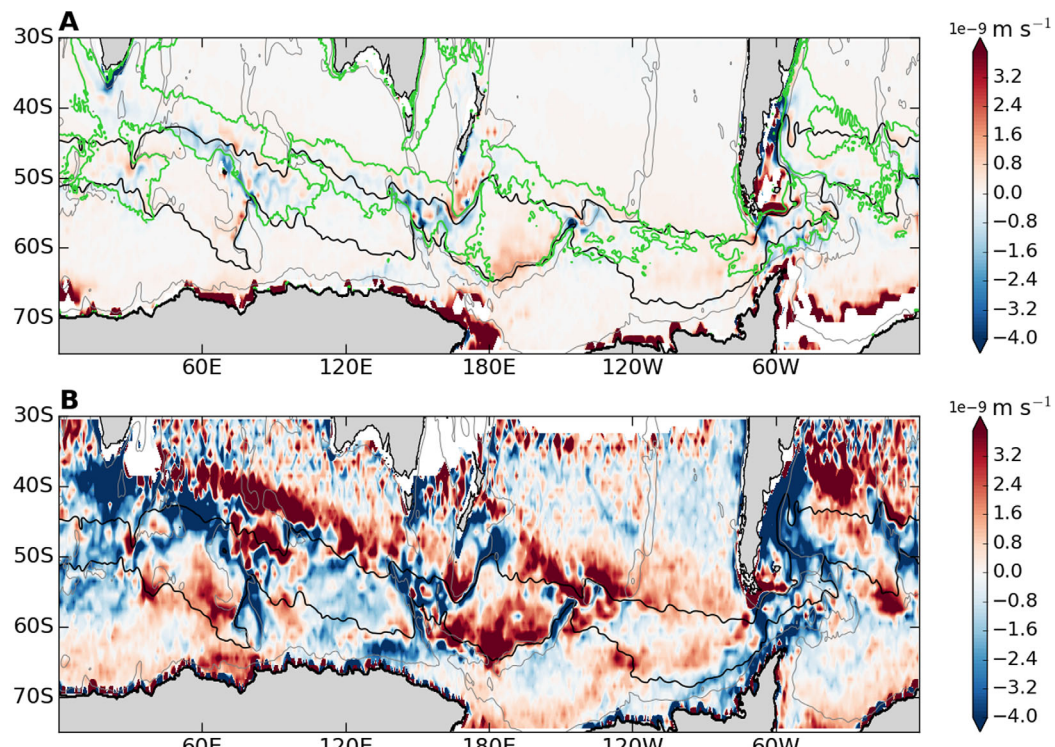


Figure 9. Ensemble averaged $d\sigma_2/dt$ in 1° longitude $\times 1^\circ$ latitude bins along particle trajectories for (a) below the SDL, (b) above the SDL (see Figure 2 for SDL density and depth). Only bins containing greater than 100 particle crossings are shown. Positive values (red) indicate increasing density. Green contours indicate regions where the mean EKE at 1000 m in SOSE is higher than $100 \text{ cm}^2 \text{s}^{-2}$, as in Figure 1d.

(Figure 9a). The weak negative transformation in the Agulhas Current and Agulhas Return Current region is likely an important contribution to the weak mean negative $\Delta\sigma_2$ at the SDL of particles originating in the Atlantic and Indian (Figure 3d) as particles from the Western Indian and Eastern Atlantic pass through this region (Figures 2a and 2b).

In order to determine which processes cause diapycnal density change, it is useful to compare the Lagrangian statistics with Eulerian estimates of transformation across density surfaces, which can be broken into contributions from surface fluxes of temperature and salt, horizontal mixing, and vertical mixing. The cumulative transformation recorded by particles could have occurred anywhere along their trajectories, which do not remain on a single density surface, so are not expected to agree precisely with the water mass transformation across a given isopycnal surface. We focus here on the Eulerian transformation on an isopycnal due to horizontal and vertical mixing, and particularly in the interior, to compare with the density changes along Lagrangian trajectories below the SDL and ML.

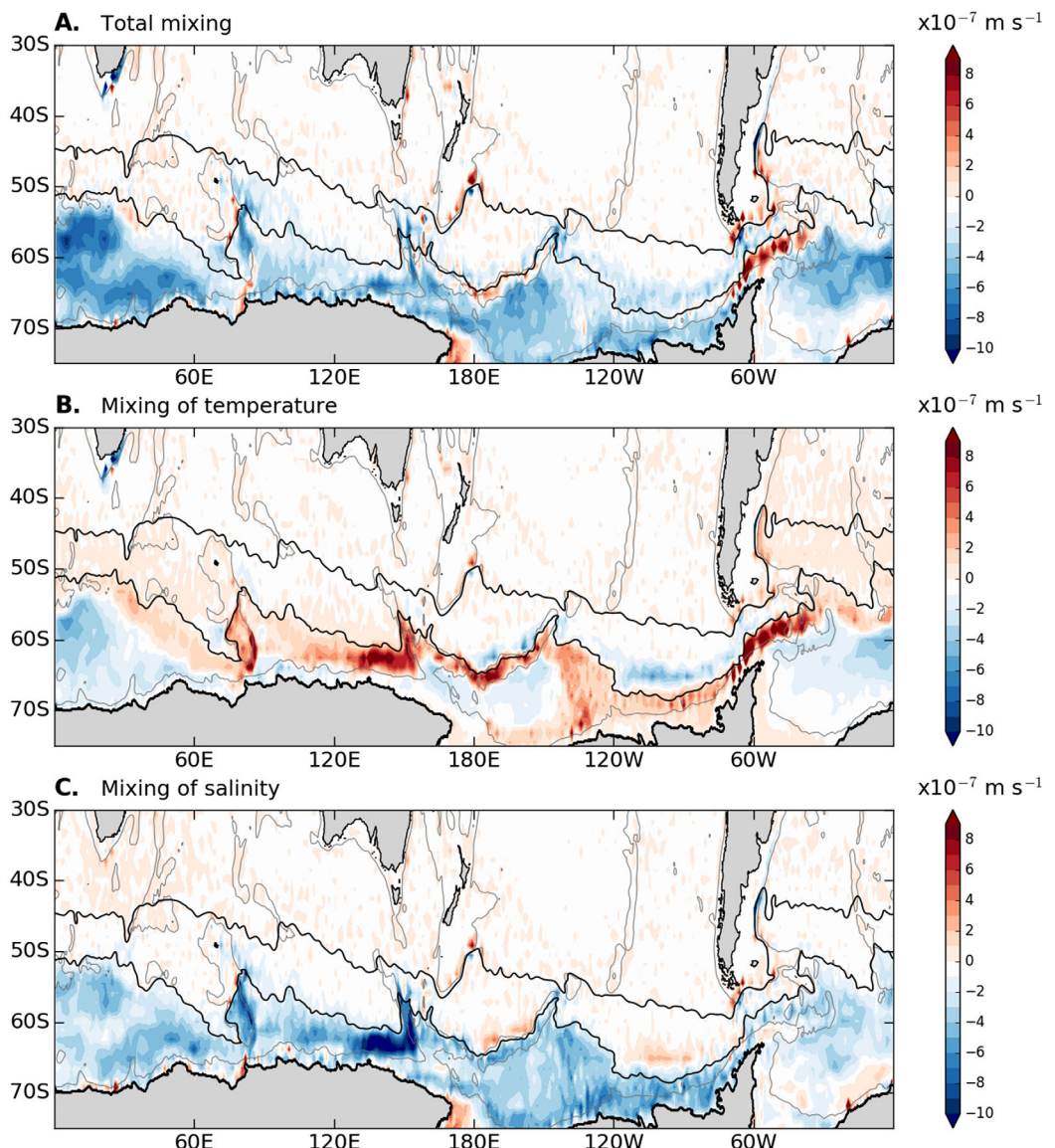


Figure 10. Mean water mass transformation (m s^{-1}) across $36.6 \text{ kg m}^{-3} < \sigma_2 < 36.8 \text{ kg m}^{-3}$ (light UCDW) due to (a) total diapycnal mixing, (b) diapycnal mixing of temperature, and (c) diapycnal mixing of salt. Grey contours in (d) and (e) show the 3,000 m bathymetry contour.

The transformation due to mixing across the $36.7 \text{ kg m}^{-3} < \sigma_2 < 36.9 \text{ kg m}^{-3}$ range (corresponding to the center of the UCDW density class) shows a very small transformation north of and within the ACC and broad negative transformation toward lighter densities south of the ACC (Figure 10). This region of negative transformation of light UCDW along the southern ACC boundary and south of the ACC encompasses the locations where most particles first outcrop into the mixed layer (Figure 1e).

This distribution is consistent with the Lagrangian distributions of σ_2 and $\Delta\sigma_2$, which show generally small transformation during interior upwelling but a distinct shift toward lighter densities as they approach the ML, which occurs predominantly south of the ACC. There are a few notable exceptions to this pattern, with significant positive transformation on the southern side of the ACC in Drake Passage, along the Pacific-Antarctic Ridge, south of Kerguelen Plateau and in the western Ross Sea. In these locations, density increase by mixing of temperature exceeds density decrease due to mixing of freshwater (Figures 10b and 10c).

The broad region of negative transformation south of the ACC is due to mixing of both temperature and salinity, although along some regions along the southern ACC boundary there is strong compensation

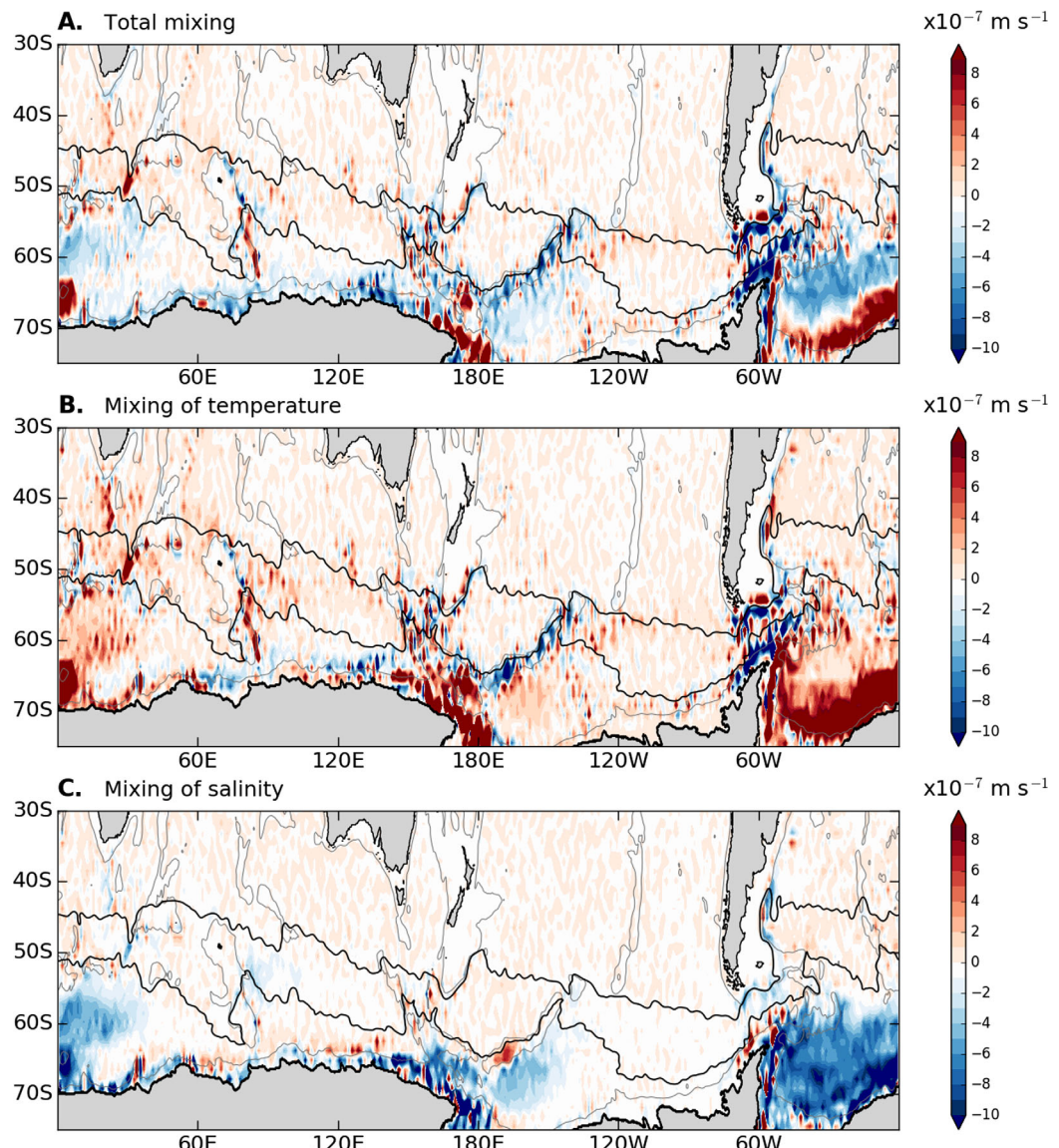


Figure 11. Water mass transformation (m s^{-1}) averaged across the $37.0 \text{ kg m}^{-3} < \sigma_2 < 37.15 \text{ kg m}^{-3}$ (LCDW) layer due to (a) total diapycnal mixing, (b) diapycnal mixing of temperature, and (c) diapycnal mixing of salt. Grey contours in (d) and (e) show the 3,000 m bathymetry contour.

between mixing of temperature and salt, with mixing of salt dominating in these locations (Figures 10b and 10c). This is generally in agreement with the Lagrangian temperature and salinity contributions to $\Delta\sigma_2$ in Figure 6. However, the $\Delta\theta$ and ΔS contributions from the Lagrangian analysis indicate that mixing of heat leads to a net increase in density for most particles, which would correspond with positive transformation, while the map of transformation due to mixing of temperature shows regions of both positive and negative transformation.

The result that mixing of freshwater is the dominant term transforming UCDW to lighter densities is consistent with previous water mass transformation analyses showing that vertical mixing of deep water with fresher waters above dominates the total mixing contribution to transformation (Abernathy et al., 2016), and leads to conversion of UCDW to IW below the ML (Iudicone et al., 2008a). Iudicone et al. (2008a) propose that this freshening occurs as UCDW is approaching the upper ocean in the region south of the ACC where upward Ekman pumping brings UCDW up to where it encounters strong salinity gradients just below the mixed layer, mixing with fresher water to gain buoyancy.

The transformation averaged over isopycnal layers for $37.0 \text{ kg m}^{-3} < \sigma_2 < 37.15 \text{ kg m}^{-3}$ (Figure 11) corresponds to the secondary peak in densities at the SDL crossing (Figure 3b) within the LCDW density class. Separating the transformation due to mixing of temperature and mixing of salt clearly shows strong compensation, consistent with the Lagrangian analysis (Figure 6). Over this density range, the impact of mixing is to very weakly increase density north of and within the ACC, with localized areas of stronger density increase and decrease south of the ACC where the isopycnals are closer to the sea surface (Figure 11). The broadly positive transformation within and north of the ACC in this range is a result of horizontal mixing (not shown) and is consistent with the Lagrangian statistics showing that particles initially in the denser LCDW density range tend to increase density in the interior, diverging from the lighter water masses during upwelling to the SDL (Figure 5). There is stronger transformation, both positive and negative, south of the ACC where the LCDW density surfaces shoal toward the surface. In particular, there is strong positive transformation near the Antarctic continent where these density surfaces outcrop, corresponding to regions of AABW formation. This densification is caused by dominance of cooling by mixing of temperature (Figure 11b) over freshening by mixing of salt (Figure 11c). Further north in the Weddell and Ross gyres, transformation by mixing of temperature is weak or even negative, indicating warming, and thus the next effect of mixing is to make water lighter in these regions.

Both the Lagrangian $d\sigma_2/dt$ in the ocean interior (Figure 9) and the Eulerian transformation (Figures 10 and 11) show coherent hot spots of enhanced density change at major topographic features (contoured in grey) where interaction of the mean flow with topography generates vigorous eddy activity. These locations at and downstream of topography are similar to the locations of maximum interior upwelling in the ACC, including the Southwest Indian Ridge, Kerguelen Plateau, Macquarie Ridge, Pacific Antarctic Ridge, and Drake Passage region (Figures 1a and 1b; Tamsitt et al., 2017). In the ocean interior far from the surface, the total diapycnal mixing is dominated by the horizontal component (not shown), which may be a result of the SOSE prescribed subgrid mixing parameterizations. Nevertheless, the interior mixing is greatly enhanced in regions with strong fronts and eddy activity, which generate strong horizontal density gradients, which with a constant diffusivity leads to larger transformation.

To quantify the contribution of eddy hot spots associated with topography to cumulative diapycnal transformation along upwelling pathways, we bin particle $d\sigma_2/dt$ by EKE levels. Using the time-mean surface EKE distribution, with the assumption that the spatial pattern of EKE is similar at all depths, we sum the absolute value of $d\sigma_2/dt$ for each particle in each $10 \text{ m}^{-2} \text{ s}^{-2}$ surface mean EKE bin, to obtain the contribution to the particle total transformation as a function of EKE (Figure 12). Comparing the cumulative RMS of particle $d\sigma_2/dt$ as a

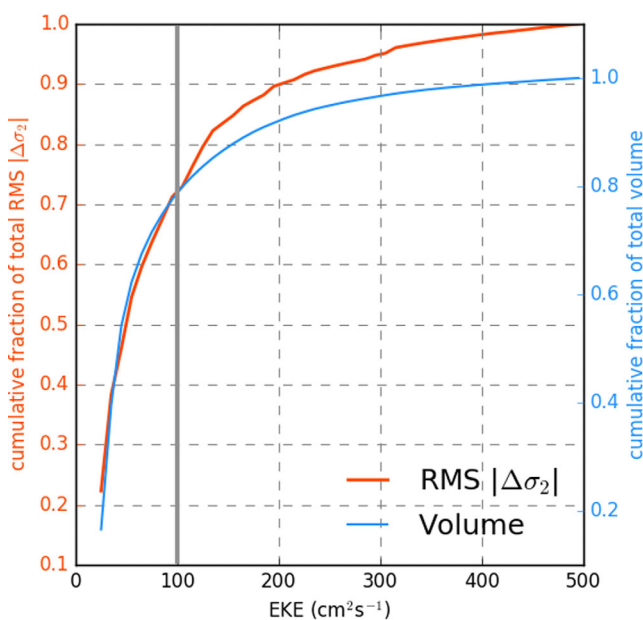


Figure 12. Cumulative fraction of total RMS of absolute density change (red), and cumulative fraction of total ocean volume (blue), as a function of EKE. Note that the limits of the two y axes differ, with the density change y axis (left) extending from 0 to 1 but the volume y axis (right) extending above 1 in order to show clearly the alignment of the two curves at low EKE values ($<100 \text{ cm}^2 \text{s}^{-2}$) and the separation at high EKE values ($>100 \text{ cm}^2 \text{s}^{-2}$). The heavy grey line at EKE = $100 \text{ cm}^2 \text{s}^{-2}$ emphasizes the point at which the two lines begin to deviate.

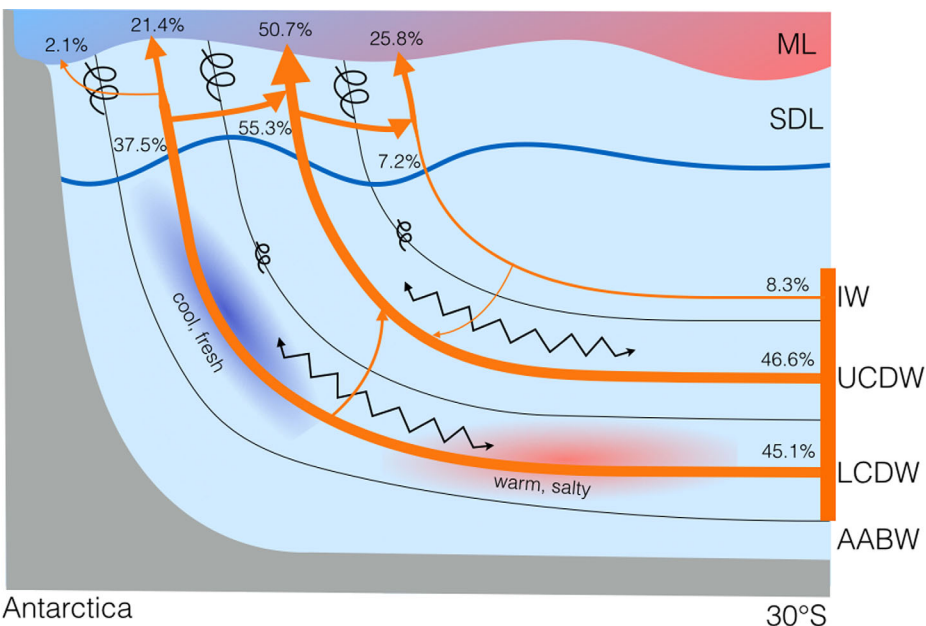


Figure 13. Schematic of the fate of upwelling deep water that travels from 30°S to the mixed layer. Grey indicates the seafloor. Black curves indicate the boundary between IW, UCDW, LCDW, and AABW density layers. The blue line is the lower boundary of the SDL and shaded region above indicates the mixed layer, with the blue to red gradient indicating the buoyancy gradient in the mixed layer. The orange bar indicates the depth range over which particles were released at 30°S between 1,000 and 3,500 m depth, with a total combined upwelling of particles represents 21.3 Sv of transport. Orange arrows indicate pathways of particles from 30°S to the ML in each density class, with wider arrows indicating a larger percentage of the total upwelling, with the corresponding percentage of total upwelling particles shown alongside the arrows at 30°S, the SDL crossing, and ML crossing (as listed in Table 1). Black zig-zag arrows indicate isopycnal mixing and black spirals indicate diapycnal mixing (weak in the interior below the SDL and stronger in the SDL). Red and blue shading on the LCDW layer indicate the along isopycnal gradient from relatively warm and salty to relatively cool and fresh.

function of EKE to the total volume in each EKE bin illustrates that areas with high EKE have disproportionately large influence on particle density change given their volume. This is clearly visible in Figure 12 by the divergence of the two lines at high EKE values (greater than $100 \text{ m}^{-2} \text{ s}^{-2}$, contoured in Figures 1d and 9). However, this divergence is small and the majority of the volume is in regions with low EKE. Therefore, close to 75% of the cumulative RMS $d\sigma_2/dt$ occurs at $\text{EKE} < 100 \text{ m}^{-2} \text{ s}^{-2}$, while the remaining 25% occurs in regions with $\text{EKE} > 100 \text{ m}^{-2} \text{ s}^{-2}$. Therefore, while most interior upwelling (i.e., crossing of depth surfaces) occurs at topographic hot spots (Figure 1d and Tamsitt et al., 2017), diapycnal change (crossing of density surfaces) is not as strongly concentrated at these hot spots. This supports the hypothesis presented by Tamsitt et al. (2017, Figure 7), that the upwelling is predominantly isopycnal in these hot spots. With this new knowledge, the Tamsitt et al. (2017) isopycnal upwelling at topographic hot spots should be modified to reflect the fact that density change along upwelling pathways the ocean interior is somewhat enhanced in the topographic hot spots, but these density changes are small relative to the transformation that occurs between the SDL and the ML.

4. Summary and Conclusions

We have quantified the cumulative water mass transformation along Southern Ocean Lagrangian upwelling pathways in the ocean interior and have summarized the overall water mass transformation and processes involved in an idealized schematic (Figure 13). In the interior, upwelling predominantly follows isopycnal surfaces up until reaching a surface diabatic layer, defined by the densest isopycnal that outcrops at a given location, above which there is strong transformation toward lighter density classes as a result of freshening due to mixing with fresher surrounding water. Despite interior density changes being relatively small, the density distribution of deep water shows a clear migration toward two separate density classes during upwelling, which indicates the early stages of the separation of upwelling waters into the upper and lower

branches of the overturning circulation, which is completed by buoyancy fluxes at the sea surface. Although the pathways are close to isopycnal, compensated changes in temperature and salinity leads to homogenization of different source deep waters by mixing with relatively cold, fresh subpolar water.

There is large seasonality of surface buoyancy fluxes and winds, particularly associated with sea ice, which may lead to seasonality in the density changes along upwelling particle trajectories. This has been shown to be important for water mass transformation due to sea ice in the Southern Ocean (Abernathy et al., 2016). Further analysis of the differences in upwelling and water mass transformation in different seasons is needed to determine how seasonal processes influence upwelling and water mass evolution along these pathways. Additionally, nonlinearities in the equation of state lead to significant water mass transformation in the Southern Ocean due to cabbeling and thermobaricity (Groeskamp et al., 2016). In particular, analysis of observations show significant LCDW formation from UCDW due to nonlinear water mass transformation (Groeskamp et al., 2016). Because most of our analysis is done using potential density, the contribution to the water mass transformation from thermobaric effects are not captured using this density coordinate. However, the qualitative agreement between results using potential density and neutral density indicates that the inclusion of thermobaricity does not change our conclusions, but more work is needed to further quantify the role of nonlinear processes in water mass transformation in upwelling pathways.

There are additional challenges to understand how Lagrangian methods can introduce errors in the density change recorded along particle trajectories, and more attention is needed to address these concerns. There are several potential sources of errors. (1) The aliasing effect: errors are introduced in the trajectory integration using 1 day mean velocity. The effect of superinertial velocity fluctuation was not taken into account. This type of error is possibly uncorrelated, meaning that it will not introduce a drift in the mean property of a cloud of particles. But it can introduce additional spreading of a cloud of particles, i.e., changing its rate of change of the second moment. However, this type of error should be small because the decorrelation time scale for balanced eddy motion in the Southern Ocean is much larger than 1 day. The deviations from the linear interpolation between daily mean velocities should be negligible comparing to the daily mean velocity. (2) The random shuffling parameterization in the mixed layer is ad hoc, without rigorous derivation. This is not an important error source in our study as we focus on particles before entering the ML. (3) The horizontal and vertical background mixing parameterizations and values used in SOSE may not represent the true ocean physics. This question is beyond the scope of Lagrangian methods alone but rather is related to numerical simulations in general, for which these parameterizations are continually evolving based on new experimental insights. (4) The Eulerian and Lagrangian models use very different numerical schemes to describe advection processes, each with distinct numerical discretization errors. Since SOSE's conservation laws are derived in an Eulerian finite-volume framework, it is unlikely that the Lagrangian particles maintain rigorous conservation of temperature and salinity the way that grid cells do. In spite of these limitations, the qualitative agreement between the Lagrangian particle and the Eulerian tracer analyses in this study validates the use of the Lagrangian method, which can provide a detailed view of the water mass pathways that is lacking in Eulerian analysis.

Our result that deep source water properties homogenize during upwelling differs somewhat from the prevailing view of NADW and IDW/PDW upwelling in the Southern Ocean interior as separate in density and property space (Talley, 2013), with denser NADW preferentially feeding into the lower cell and IDW/PDW preferentially entering the upper cell. However, despite the homogenization in properties and broad overlap in the density distribution of Atlantic, Indian and Pacific deep waters, our results do show that the mean of the NADW density distribution remains slightly denser than Indo-Pacific deep waters, and this difference is preserved throughout the transformation that occurs during upwelling. An important caveat to our result is that we consider only particles that upwell all the way to the mixed layer, and thus do not capture deep water that is transformed into AABW in the interior, entering the lower cell without upwelling to the sea surface. It is possible that analysis of all deep water trajectories entering the Southern Ocean may show a preferential conversion of denser NADW into AABW in the interior, and further work is needed to investigate transformation of deep waters into AABW. In addition, as with many other ocean models with similar resolution, SOSE underestimates the rate of AABW formation processes, thus more detailed analysis of this transformation should be investigated in models that better capture AABW formation.

Here we show that although upwelling predominantly follows isopycnals in the ocean interior, the distinct salty, warm signature of NADW is eroded by density-compensated mixing with colder, fresher water during

upwelling through the Southern Ocean interior prior to the influence of surface buoyancy fluxes, leading to homogenization of deep water properties. This result parallels findings from Lagrangian analysis of outflow pathways of AABW, which also show homogenization of distinct source water properties (Van Sebille et al., 2013). At the same time, the overall divergence of densities during interior upwelling into a dominant UCDW water mass and a distinct smaller, dense, LCDW water mass shows the role of interior diapycnal mixing in initializing the water mass transformation necessary for the Southern Ocean upper and lower overturning cells, the rest of which is accomplished by buoyancy fluxes at the surface.

While the instantaneous rate of density change experienced by a particle at topographic hot spots in the ocean interior is elevated compared to elsewhere, the small volume extent of these hot spots, and relatively small amount of time particles spend in these regions means that the majority of cumulative density change along upwelling pathways in the ocean interior occurs as a result of background mixing, consistent with the results of Holzer and Primeau (2006). Additionally, the cumulative transformation in the ocean interior (below the SDL) is dwarfed by density changes influenced by surface fluxes in the upper ocean prior to reaching the mixed layer. In the context of Tamsitt et al. (2017), these results indicate that while upwelling across depth surfaces is strongly concentrated at hot spots associated with topography, *diapycnal* upwelling across density surfaces is less clearly enhanced at these hot spots. However, SOSE lacks sufficient vertical resolution to resolve the bottom boundary layer, and does not parameterize lee wave driven mixing, and thus is missing important boundary processes that may contribute significantly to the modification of LCDW. While it is well understood that eddy stirring brings water in contact with intense mixing close to topographic features, recent work from tracer release experiments also suggests that slow mean flows and recirculating eddies trap tracers near topography for long times, increasing the amount of mixing in these hot spots (Mashayek et al., 2017). We have shown in the model that in the ocean interior, there are hot spots of density change at or downstream of topographic features and relative density change is somewhat elevated in regions with high EKE. In reality, water parcels upwelling along major ridges and plateaus are likely to interact with the bottom boundary layer, experiencing more mixing that is not resolved in this model. Thus, we hypothesize that topographic hot spots contribute a greater fraction of the total density change in the ocean interior than reported here. Further research using observations and Lagrangian experiments in higher resolution models are necessary to fully determine the role of mixing hot spots in transformation of upwelling deep water.

Acknowledgments

V.T., R.P.A., and L.D.T. were supported by NSF OCE-1357072. R.P.A. acknowledges support from NSF grant OCE-1357133. M.R.M. is supported by NSF award PLR-1425989. J.W. acknowledges support from NSF OCE-1234473 and declares that this work was done as a private venture and not in the author's capacity as an employee of the Jet Propulsion Laboratory, California Institute of Technology. We acknowledge high-performance computing support from Yellowstone (ark:/85065/d7wd3xhc) provided by NCARs Computational and Information Systems Laboratory, sponsored by the National Science Foundation, and from the Yeti HPC cluster, provided by Columbia University Research Computing Services. SOSE Iteration 100 model output is available at <http://sose.ucsd.edu>. Lagrangian trajectories used in this paper are available from the corresponding author upon request. The authors Sjoerd Groeskamp and one anonymous reviewer whose comments greatly improved the manuscripts and thank H. Drake and A. Morrison for extensive discussions on the Lagrangian analysis, and I. Cerovečki for useful discussion on water mass transformation.

The transformation of upwelling deep water masses in the Southern Ocean has important implications for the fate of nutrients and carbon, as most of the deep carbon and nutrient reservoir enters the Southern Ocean via the Indian and Pacific. Further work is needed to determine how these upwelling pathways supply natural carbon from the deep ocean to the sea surface and the influence of interior mixing on the pathways and rates.

References

- Abernathy, R. P., Cerovecki, I., Holland, P. R., Newsom, E., Mazloff, M., & Talley, L. D. (2016). Water-mass transformation by sea ice in the upper branch of the Southern Ocean overturning. *Nature Geoscience*, 9, 596–601. <https://doi.org/10.1038/ngeo2749>
- Adcroft, A., Hill, C., & Marshall, J. (1997). Representation of topography by shaved cells in a height coordinate ocean model. *Monthly Weather Review*, 125(9), 2293–2315.
- Ballarotta, M., Drijfhout, S., Kuhlbrodt, T., & Döös, K. (2013). The residual circulation of the Southern Ocean: Which spatio-temporal scales are needed? *Ocean Modelling*, 64, 46–55.
- Brambilla, E., Talley, L. D., & Robbins, P. E. (2008). Subpolar mode water in the northeastern Atlantic: 2. Origin and transformation. *Journal of Geophysical Research*, 113, C04026. <https://doi.org/10.1029/2006JC004063>
- Bryan, F., & Bachman, S. (2015). Isohaline salinity budget of the North Atlantic salinity maximum. *Journal of Physical Oceanography*, 45(3), 724–736.
- Cerovečki, I., & Marshall, J. (2008). Eddy modulation of air-sea interaction and convection. *Journal of Physical Oceanography*, 38, 65–93.
- Cerovečki, I., Mazloff, M. R., & Talley, L. D. (2011). A comparison of Southern Ocean air-sea buoyancy flux from an ocean state estimate with five other products. *Journal of Climate*, 24(24), 6283–6306. <https://doi.org/10.1175/2011JCLI3858.1>
- Cook, A., Holland, P., Meredith, M., Murray, T., Luckman, A., & Vaughan, D. (2016). Ocean forcing of glacier retreat in the western antarctic peninsula. *Science*, 353(6296), 283–286.
- Dee, D. P., Uppala, S. M., Simmons, A. J., Berrisford, P., Poli, P., Kobayashi, S., et al. (2011). The ERA-Interim reanalysis: Configuration and performance of the data assimilation system. *Quarterly Journal of the Royal Meteorological Society*, 137, 553–597. <https://doi.org/10.1002/qj.828>
- Döös, K., Nilsson, J., Nylander, J., Brodeau, L., & Ballarotta, M. (2012). The World Ocean thermohaline circulation. *Journal of Physical Oceanography*, 42(9), 1445–1460.
- Döös, K., Nylander, J., & Coward, A. C. (2008). Lagrangian decomposition of the Deacon Cell. *Journal of Geophysical Research*, 113, C07028. <https://doi.org/10.1029/2007JC004351>

- Downes, S. M., Gnanadesikan, A., Griffies, S. M., & Sarmiento, J. L. (2011). Water mass exchange in the Southern Ocean in coupled climate models. *Journal of Physical Oceanography*, 41(2001), 1756–1771. <https://doi.org/10.1175/2011JPO4586.1>
- Forget, G. (2010). Mapping ocean observations in a dynamical framework: A 2004–06 ocean atlas. *Journal of Physical Oceanography*, 40(6), 1201–1221. <https://doi.org/10.1175/2009JPO4043.1>
- Foster, T. D. (1972). An analysis of the cabbeling instability in sea water. *Journal of Physical Oceanography*, 2(3), 294–301.
- Frölicher, T. L., Sarmiento, J. L., Paynter, D. J., Dunne, J. P., Krasting, J. P., & Winton, M. (2015). Dominance of the Southern Ocean in anthropogenic carbon and heat uptake in CMIP5 models. *Journal of Climate*, 28(2), 862–886. <https://doi.org/10.1175/JCLI-D-14-00117.1>
- Ganachaud, A., & Wunsch, C. (2000). Improved estimates of global ocean circulation, heat transport and mixing from hydrographic data. *Nature*, 408(6811), 453.
- Garabato, A. C. N., Polzin, K. L., King, B. A., Heywood, K. J., & Visbeck, M. (2004). Widespread intense turbulent mixing in the Southern Ocean. *Science*, 303(5655), 210–213.
- Groeskamp, S., Abernathy, R. P., & Klocker, A. (2016). Water mass transformation by cabbeling and thermobaricity. *Geophysical Research Letters*, 43, 10835–10845. <https://doi.org/10.1002/2016GL070860>
- Groeskamp, S., Sloyan, B. M., Zika, J. D., & McDougall, T. J. (2017). Mixing inferred from an ocean climatology and surface fluxes. *Journal of Physical Oceanography*, 47(3), 667–687.
- Groeskamp, S., Zika, J. D., Sloyan, B. M., McDougall, T. J., & McIntosh, P. C. (2014). A thermohaline inverse method for estimating diathermal circulation and mixing. *Journal of Physical Oceanography*, 44(10), 2681–2697. <https://doi.org/10.1175/JPO-D-14-0039.1>
- Holte, J., & Talley, L. (2009). A new algorithm for finding mixed layer depths with applications to argo data and subantarctic mode water formation. *Journal of Atmospheric and Oceanic Technology*, 26(9), 1920–1939. <https://doi.org/10.1175/2009TECHO543.1>
- Holzer, M., & Primeau, F. W. (2006). The diffusive ocean conveyor. *Geophysical Research Letters*, 33, L14618. <https://doi.org/10.1029/2006GL026232>
- Iudicone, D., Madec, G., Blanke, B., & Speich, S. (2008a). The role of Southern Ocean surface forcings and mixing in the global conveyor. *Journal of Physical Oceanography*, 38(7), 1377. <https://doi.org/10.1175/2008JPO3519.1>
- Iudicone, D., Madec, G., & McDougall, T. J. (2008c). Water-mass transformations in a neutral density framework and the key role of light penetration. *Journal of Physical Oceanography*, 38, 1357–1376. <https://doi.org/10.1175/2007JPO3464.1>
- Iudicone, D., Speich, S., Madec, G., & Blanke, B. (2008b). The global conveyor belt from a Southern Ocean perspective. *Journal of Physical Oceanography*, 38(7), 1401–1425. <https://doi.org/10.1175/2007JPO3525.1>
- Jackett, D. R., & McDougall, T. J. (1995). Minimal adjustment of hydrographic profiles to achieve static stability. *Journal of Atmospheric and Oceanic Technology*, 12(2), 381–389.
- Katsumata, K., Sloyan, B., & Masuda, S. (2013). Diapycnal and isopycnal transports in the Southern Ocean estimated by a box inverse model. *Journal of Physical Oceanography*, 43(11), 2270–2287.
- Klocker, A., & McDougall, T. J. (2010). Influence of the nonlinear equation of state on global estimates of dianeutral advection and diffusion. *Journal of Physical Oceanography*, 40(8), 1690–1709.
- Kunze, E., Firing, E., Hummon, J. M., Chereskin, T. K., & Thurnherr, A. M. (2006). Global abyssal mixing inferred from lowered adcp shear and ctd strain profiles. *Journal of Physical Oceanography*, 36(8), 1553–1576.
- Large, W. G., McWilliams, J. C., & Doney, S. C. (1994). Oceanic vertical mixing: A review and a model with a nonlocal boundary layer parameterization. *Reviews of Geophysics*, 32(4), 363–403. <https://doi.org/10.1029/94RG01872>
- Ledwell, J., Montgomery, E., & Polzin, K. (2000). Evidence for enhanced mixing over rough topography in the abyssal ocean. *Nature*, 40(1988), 13–16.
- Lumpkin, R., & Speer, K. (2007). Global ocean meridional overturning. *Journal of Physical Oceanography*, 37(10), 2550–2562. <https://doi.org/10.1175/JPO3130.1>
- Marshall, J., Jamous, D., & Nilsson, J. (1999). Reconciling thermodynamic and dynamic methods of computation of water-mass transformation rates. *Deep Sea Research Part I: Oceanographic Research Papers*, 46(4), 545–572.
- Mashayek, A., Ferrari, R., Merrifield, S., Ledwell, J. R., St Laurent, L., & Garabato, A. N. (2017). Topographic enhancement of vertical turbulent mixing in the Southern Ocean. *Nature Communications*, 8, 14197. <https://doi.org/10.1038/ncomms14197>
- Mazloff, M. R., Heimbach, P., & Wunsch, C. (2010). An eddy-permitting Southern Ocean State Estimate. *Journal of Physical Oceanography*, 40(5), 880–899. <https://doi.org/10.1175/2009JPO4236.1>
- McDougall, T. J., & Barker, P. M. (2011). *Getting started with TEOS-10 and the Gibbs Seawater (GSW) oceanographic toolbox* (Rep. SCOR/IAPSO WG127, pp. 1–28). Scientific Committee on Oceanic Research.
- McDougall, T. J., & Jackett, D. R. (2005). The material derivative of neutral density. *Journal of Marine Research*, 63(1), 159–185.
- Munk, W. (1966). Abyssal recipes. *Deep Sea Research and Oceanographic Abstracts*, 13, 707–730.
- Munk, W., & Wunsch, C. (1998). Abyssal recipes II: Energetics of tidal and wind mixing. *Deep Sea Research Part I: Oceanographic Research Papers*, 45(12), 1977–2010.
- Naveira Garabato, A. C., Polzin, K. L., Ferrari, R., Zika, J. D., & Forryan, A. (2016). A microscale view of mixing and overturning across the Antarctic Circumpolar Current. *Journal of Physical Oceanography*, 46(1), 233–254.
- Nikurashin, M., & Ferrari, R. (2013). Overturning circulation driven by breaking internal waves in the deep ocean. *Geophysical Research Letters*, 40, 3133–3137. <https://doi.org/10.1002/grl.50542>
- Nikurashin, M., & Vallis, G. (2011). A theory of deep stratification and overturning circulation in the ocean. *Journal of Physical Oceanography*, 41(3), 485–502.
- Polzin, K. L. (1997). Spatial variability of turbulent mixing in the abyssal ocean. *Science*, 276(5309), 93–96. <https://doi.org/10.1126/science.276.5309.93>
- Ruan, X., Thompson, A. F., Flexas, M. M., & Sprintall, J. (2017). Contribution of topographically generated submesoscale turbulence to Southern Ocean overturning. *Nature Geoscience*, 10, 840–845.
- Sarmiento, J. L., Gruber, N., Brzezinski, M. A., & Dunne, J. P. (2004). High-latitude controls of thermocline nutrients and low latitude biological productivity. *Nature*, 427, 56–60. <https://doi.org/10.1038/nature02127>
- Sloyan, B. M., & Rintoul, S. R. (2000). Estimates of area-averaged diapycnal fluxes from basin-scale budgets. *Journal of Physical Oceanography*, 30(9), 2320–2341.
- Sloyan, B. M., & Rintoul, S. R. (2001). The Southern Ocean limb of the global deep overturning circulation. *Journal of Physical Oceanography*, 31(1), 143–173.
- Speer, K., Rintoul, S. R., & Sloyan, B. (2000). The diabatic deacon cell. *Journal of Physical Oceanography*, 30, 3212–3222. [https://doi.org/10.1175/1520-0485\(2000\)030<3212:TDC>2.0.CO;2](https://doi.org/10.1175/1520-0485(2000)030<3212:TDC>2.0.CO;2)
- St. Laurent, L., Naveira Garabato, A. C., Ledwell, J. R., Thurnherr, A. M., Toole, J. M., & Watson, A. J. (2012). Turbulence and diapycnal mixing in Drake Passage. *Journal of Physical Oceanography*, 42(12), 2143–2152.

- Stewart, K. D., & Haine, T. W. (2016). Thermobaricity in the transition zones between alpha and beta oceans. *Journal of Physical Oceanography*, 46(6), 1805–1821.
- Talley, L. D. (2013). Closure of the global overturning circulation through the Indian, Pacific, and Southern Oceans: Schematics and transports. *Oceanography*, 26(1), 80–97. <https://doi.org/10.5670/oceanog.2013.07>
- Tamsitt, V., Drake, H., Morrison, A., Talley, L. D., Dufour, C., Gray, A., et al. (2017). Spiraling up: pathways of global deep water from the deep ocean to the surface of the Southern Ocean. *Nature Communications*, 8, 172.
- Tamsitt, V., Talley, L. D., Mazloff, M. R., & Cerovečki, I. (2016). Zonal variations in the Southern Ocean heat budget. *Journal of Climate*, 29(18), 6563–6579.
- Toggweiler, J., Samuels, B. (1998). On the ocean's large-scale circulation near the limit of no vertical mixing. *Journal of Physical Oceanography*, 9, 1832–1852.
- Van Sebille, E., Johns, W. E., & Beal, L. M. (2012). Does the vorticity flux from Agulhas rings control the zonal pathway of NADW across the South Atlantic? *Journal of Geophysical Research*, 117, C05037. <https://doi.org/10.1029/2011JC007684>
- Van Sebille, E., Spence, P., Mazloff, M. R., England, M. H., Rintoul, S. R., & Saenko, O. A. (2013). Abyssal connections of Antarctic Bottom Water in a Southern Ocean State Estimate. *Geophysical Research Letters*, 40, 2177–2182. <https://doi.org/10.1002/grl.50483>
- Walsh, G. (1982). On the relation between sea-surface heat flow and thermal circulation in the ocean. *Tellus*, 34(2), 187–195.
- Waterhouse, A. F., MacKinnon, J. A., Nash, J. D., Alford, M. H., Kunze, E., Simmons, H. L., et al. (2014). Global patterns of diapycnal mixing from measurements of the turbulent dissipation rate. *Journal of Physical Oceanography*, 44(7), 1854–1872.
- Watson, A. J., Ledwell, J. R., Messias, M.-J., King, B. A., Mackay, N., Meredith, M. P., et al. (2013). Rapid cross-density ocean mixing at mid-depths in the Drake Passage measured by tracer release. *Nature*, 501(7467), 408–411. <https://doi.org/10.1038/nature12432>
- Whalen, C. B., Talley, L. D., & MacKinnon, J. A. (2012). Spatial and temporal variability of global ocean mixing inferred from Argo profiles. *Geophysical Research Letters*, 39, L18612. <https://doi.org/10.1029/2012GL053196>
- Wolfe, C. L., & Cessi, P. (2011). The adiabatic pole-to-pole overturning circulation. *Journal of Physical Oceanography*, 41(9), 1795–1810.
- Young, W. R. (2012). An exact thickness-weighted average formulation of the boussinesq equations. *Journal of Physical Oceanography*, 42(5), 708–724.
- Zika, J. D., McDougall, T. J., & Sloyan, B. M. (2010). A tracer-contour inverse method for estimating ocean circulation and mixing. *Journal of Physical Oceanography*, 40(1), 26–47.